THE PENNSYLVANIA STATE UNIVERSITY
SCHREYER HONORS COLLEGE

DEPARTMENT OF METEOROLOGY

USING LABORATORY MEASURMENTS OF VAPOR-GROWN ICE CRYSTALS

TO INFER SURFACE KINETICS AND ESTIMATE THE DEPOSITION COEFFICIENT

GWENORE POKRIFKA
SPRING 2018

A thesis
submitted in partial fulfillment
of the requirements
for a baccalaureate degree
in Meteorology
with honors in Meteorology

Reviewed and approved* by the following:

Jerry Y. Harrington
Professor of Meteorology
Thesis Supervisor

Yvette Richardson
Professor of Meteorology
Associate Dean for Undergraduate Education, College of EMS
Honors Adviser

* Signatures are on file in the Schreyer Honors College.

ABSTRACT

The vapor growth of ice crystals has long been misrepresented in cloud and climate models. Ice crystals growing from water vapor are limited by both the diffusion of vapor to the particle and the kinetics of surface attachment, the latter of which model parameterizations typically ignore. Model parameterizations' incompleteness is in part due to an incomplete understanding of surface attachment kinetics, which are often represented by a growth efficiency known as the deposition coefficient. This work seeks to improve understanding of the deposition coefficient by studying mass growth from vapor of ten ice particles formed from frozen pure water in a levitation diffusion chamber at temperatures between -43.4 and -40.2 ℃. The data are analyzed using a diffusion-kinetics model to predict the particles' deposition coefficients, and it is found that the model cannot replicate some of the growth rates in the data timeseries. Thus, two new analysis methods are developed to eliminate the deposition coefficient's dependence on the ice supersaturation, which is uncertain. Estimates of the deposition coefficients using the new analysis methods for five ice particles are in the range of 0.018 – 0.066, 0.008 – 0.02, 0.001, 0.048 – 0.5, and 0.006 – 0.014. These particles can be modeled by a classical, faceted growth method. The remaining ice particles demonstrate growth features linked to ice crystal surface transitions. These particles' growth timeseries cannot be modeled with a classical growth method, instead requiring variable growth mechanisms in time. Surface transitions cause the deposition coefficient to change rapidly, and they may be responsible for discrepancies in past deposition coefficient measurements.

TABLE OF CONTENTS

LIST OF FIGURES

LIST OF TABLES

ACKNOWLEDGEMENTS

Chapter 1

Introduction and Background

Understanding the growth of ice crystals from vapor is imperative to understanding the development of cold clouds. Cold clouds form in regions of the atmosphere where the temperature is below the melting point of water (0 °C). Cold clouds play an integral role in producing precipitation and determining Earth's radiative budget (Chen and Lamb, 1994). Since cold clouds affect both the environment and everyday life, we need to understand how their constituent ice crystals initially form and grow. Despite their importance, the details of ice particle growth are not well understood.

Ice particle growth is complex; though the particles may share similar beginnings, such as frozen water droplets, they grow into a wide array of shapes and sizes. Further consideration for growth from vapor must be made for ice clouds, because unlike liquid-phase clouds, vapor growth alone is enough to produce precipitation-size particles (Pruppacher and Klett, 1997). Thus, vapor-grown ice is directly linked to all other ice microphysical processes, including nucleation, aggregation, riming, and precipitation formation. The underlying structure of ice follows a hexagonal prism form at atmospheric temperatures and pressures, and single crystals have two basal (hexagonal) facets and six prism (rectangular) facets, ranging in shape from thin needles to flat dendrites. It has been well established that the environment's temperature and supersaturation dictate the crystal habit, at least at temperatures T ≥ -20 °C (Figure 1.1 from Libbrecht, 2003). However, little is known about the physical mechanisms responsible for this habit diagram. The habit diagram even lacks any phenomenological explanation (Libbrecht, 2005).

Laboratory studies have been critical for developing an empirical and theoretical understanding of ice crystal growth. They have also simplified mathematical frameworks for estimating rates of axis and mass growth. Although a relatively large number of laboratory studies exist for T ≥ -20 °C, which is comparatively warm for a cold cloud, few laboratory measurements of early ice vapor growth exist for temperatures below -30 °C, and almost none exist for T < -40 °C. It is perhaps not surprising that habit diagrams conspicuously end at about -40 °C (Figure 1.1 and Lamb and Verlinde, 2011). This is worth noting because high cirrus clouds generally have T ≤ -35 °C where water can homogeneously freeze. Consequently, our knowledge of ice vapor growth is most lacking in the temperature range where ice is particularly common.

1.1 Theories and Measurements of Vapor-grown Ice

A few models have been developed in an attempt to describe ice particle growth from vapor. The classic capacitance growth model determines the ice particle's growth from the diffusion of water vapor to the particle surface for particles of various shapes (Pruppacher and Klett, 1997). This process is a function of the temperature, pressure, partial pressure of water vapor, the particle's size, and its shape. The model accounts for the diffusion of gaseous vapor molecules through "dry" air molecules to reach and deposit onto the particle surface. However, this model has two highly fallacious assumptions (Lamb and Verlinde, 2011). First, it assumes that the ice particle's surface always is rough on the nanometer scale, such that all of the impinging vapor molecules are incorporated into the bulk particle structure. Second, growth based purely on diffusion, which is known as diffusion-limited growth, cannot change the particle's aspect ratio (Nelson, 1994, pg 83). Models have approximate methods for dealing with this fundamental

problem, such as distributing mass over the crystal surface based on laboratory-determined ratios of deposition coefficients (Chen and Lamb, 1994; Harrington et al., 2013) or using mass-dimensional relationships (e.g., Walko et al., 1995; Woods et al., 2008). At liquid saturation, the Chen and Lamb (1994) deposition coefficient ratio method seems to work accurately, but it often fails at lower ice supersaturations (Zhang and Harrington, 2014). This clearly indicates a general flaw in the framework of the capacitance model, as ice crystals develop into hexagonal prisms and other shapes. As a result, the capacitance model predicts growth that is inconsistent with what is seen in most laboratory measurements and the atmosphere (e.g., Bailey and Hallett, 2009; Zhang and Harrington, 2014).

The main flaw with the capacitance growth model is that it assumes a constant vapor density over the surface and, therefore, explicitly ignores surface attachment kinetics, which are illustrated in Figure 1.2. For the vapor density to be constant over the ice crystal, the surface must be rough on a molecular scale. This typically only occurs when the crystal's temperature exceeds the roughening transition temperature, which is thought to be about -1.3 °C on the prism facet (Elbaum, 1991). When ice is not molecularly rough, vapor molecules that have diffused to the ice surface must first adsorb to the surface. At this point, the molecules diffuse across the ice surface until they either desorb from the surface or encounter ledges, or "kink sites", into which they can incorporate as a part of the ice lattice. As a result, the ice particle's surface structure influences the ratio of the number of vapor molecules incorporated into the ice particle to the number of vapor molecules impinging on the particle's surface. This ratio, known as the "deposition coefficient", α, can be interpreted as a growth efficiency ranging from zero to unity. An ice particle with an α of unity across the entire surface, which would be either a "rough" surface or one that has a high density of surface ledges, follows diffusion-limited growth. However, if α is very low, then the

particle's growth is determined primarily by surface attachment kinetics, and it is referred to as "kinetics-limited" growth. Most particles have growth rates between these two extrema, which are therefore identified to have "diffusion-kinetics limited" growth.

Several theories and models have been developed in the past to expressly calculate diffusion-kinetics limited ice particle growth (Nelson and Baker, 1996; Wood et al., 2001, Zhang and Harrington, 2014). These models solve some of the problems with the capacitance growth model. In numerical cloud models, and some laboratory studies, the typical diffusion-kinetics limited model assumes a constant value for the deposition coefficient and uses that value in tandem with the capacitance model (Gierens, 2003; Magee et al., 2006; Harrington et al., 2009; Skrotzki et al., 2013). This allows the modeled ice particle to have a reduced growth efficiency, as seen in nature, but it cannot account for the changes in growth efficiency required for different ice crystal shapes to emerge in time. Some laboratory studies have implicitly justified the use of a constant deposition coefficient due to the small sizes of their particles grown (Magee et al., 2006, Skrotzki et al., 2013). The issue here is that not all ice particles have the same deposition coefficient. In fact, it is not constant across the entire particle, but varies for each facet (Lamb and Scott, 1974). The constant deposition coefficient model can only be strictly correct for a small range of temperature, supersaturation, particle size, and ice crystal surface structure.

The results of past laboratory studies investigating constant deposition coefficient values have been scattered, especially with temperature (Skrotzki et al., 2013). This is also true of measurements taken by our group (Figure 1.3, Harrington et al., 2018). Additionally, these measurements have not been consistent in the type of ice studied. For example, measurements of the deposition coefficient on flat ice surfaces in very cold ($T < $ -70 °C), near-vacuum conditions determined α to high and > 0.3 (Haynes et al., 1992; Brown et al., 1996; Pratte et al., 2006; Kong

et al., 2014). Other studies have instead measured the growth or sublimation of individual ice particles, and their deposition coefficient values tend to be low. Measurements made by Choularton and Latham (1977) of sublimating small ice spheres at -37 °C found the deposition coefficient to be about 0.001. On the other hand, large, frozen droplets grown on a substrate measured by Korolev et al. (2004) had α values of almost unity. However, some studies of the deposition coefficient have measured individual, small, growing frozen droplets in levitation chambers, which avoids thermal effects from the substrate: Magee et al. (2006) and Harrison et al. (2016) both found that, at low temperatures (-60 to -31 °C), levitated particles had small deposition coefficients (0.001 to 0.1). Furthermore, a single value of α was not sufficient to fit the data of Magee et al. (2006). Other studies of the deposition coefficient measured the growth of crystal populations, but they too lack consistency. For instance, Earle et al. (2010) homogeneously froze ice particles and estimated a low α of 0.031. Conversely, Skrotzki et al. (2013) used a cloud chamber to study the formation of ice on aerosol and found fairly high deposition coefficients of 0.2 to 0.7. There are many potential sources for the discrepancies between these results, including the state of the ice surface being studied, different measurement techniques, size and supersaturation dependencies, nucleation on heterogeneous particles, and polycrystalline ice containing grain boundaries to serve as sources of dislocations.

The results of the studies discussed above are difficult to interpret, as they all measured the ice in different states. For example, some measurements used nearly equilibrated ice. The surfaces of equilibrated and growing ice behave differently as ledges will form and propagate across growth surfaces, but equilibrium surfaces are static and crystal edges tend to round over time. This key difference likely alters the measured deposition coefficient. If one assumes that all atmospheric ice eventually grows by surface ledges, which is arguably both reasonable and likely general, then

the deposition coefficient can be computed by theoretical (Burton et al., 1951; Lewis, 1974) and

parametric (Lamb and Chen, 1995; Nelson and Knight, 1996) models. One such model that

accounts for the deposition coefficient is to parameterize it as

$$\alpha = \left(\frac{S_{local}}{S_{crit}}\right)^{M} \tanh\left[\left(\frac{S_{crit}}{S_{local}}\right)^{M}\right], \tag{1.1}$$

where α is the deposition coefficient, S_{local} is the supersaturation at the ice surface, S_{crit} is the

critical supersaturation that controls the formations and density of surface growth ledges, and M

is a growth mechanism parameter. The value of M allows for either strong or weak α dependence

on S_{local} that is unique to the ice particle's growth conditions (Figure 1.4 from Zhang and

Harrington, 2015).

An important part of determining the deposition coefficient is its dependence on the critical

supersaturation. Published measurements of the critical supersaturation exist for temperatures as

low as -40 °C, and a composite of all known measurements by our group is shown in Figure 1.5

(Harrington et al., 2018). Nelson and Knight (1998) determined that, above temperatures of -20

°C, the variation of S_{crit} with temperature on the basal and prism facets is consistent with primary

ice habits, ranging from about 0.2% to 2.0%. The S_{crit} between -25 and -15 °C was found to be

between 2.0% and 5.0% by Bacon et al. (2003). Not many measurements of the critical

supersaturation exist for temperatures below -20 °C, but the measurements from Libbrecht et al.

(2003) and Libbrecht and Rickerby (2013) suggest that S_{crit} increases as temperature declines. The

results of these measurements and Equation 1.1 indicate that the deposition coefficient has a strong

supersaturation dependence.

One drawback faced by many laboratory studies is that small uncertainties in the ice

particles' mass or environmental conditions, such as the supersaturation, may produce large

uncertainties when determining the deposition coefficient. This issue stems from α being defined on a logarithmic scale. As a result, it is possible to misinterpret kinetics-limited growth as diffusion-limited. This problem of uncertainty on α will be explored in more depth in Section 2.5.

In Equation 1.1, Nelson and Baker (1996) suggest that M ranges from 1 to 30, depending on the surface attachment mechanism. For instance, an $M = 1$ signifies that the ice lattice has a permanent a dislocation, which produces spiral growth on the surface and many attachment sites. An example of this is shown in Figure 1.6b. As a result, α approaches unity rapidly, or the diffusion limit, as S_{local} increases (Figure 1.4a). Conversely, an M between 10 and 30 represents two-dimensional (2D) ledge nucleation, shown in Figure 1.6a. In this case, the ice surface has few attachment sites when $S_{local} < S_{crit}$, resulting in a small α, and therefore kinetics-limited growth. However, if $S_{local} > S_{crit}$, then ledges nucleate on the ice surface and serve as the attachment sites necessary to drive the deposition coefficient to unity.

The only models of atmospheric relevance that include surface attachment kinetics are the cylinder model of Nelson and Baker (1996), the hexagonal prism model of Wood et al., (2001), and the Kinetics-Limited Adaptive Habit (KLAH) model of Zhang and Harrington (2014). The Nelson and Baker (1996) and Wood et al. (2001) models are consistent with the growth of ice crystals with relatively sharp edges, which best represents reality, but they are restrictive since they are applicable to only a single shape. Conversely, the KLAH model uses the capacitance model to describe the far-field diffusion fluxes coupled with a constant flux surface model. Although the KLAH model is not consistent in its treatment of the far-field diffusion coupling with the surface, it does capture the main features of ice crystal growth and is general enough to apply to a variety of ice particle shapes (Zhang and Harrington, 2014). The KLAH model incorporates the parameterization of the deposition coefficient given in Equation 1.1 and therefore predicts the

deposition coefficients for the basal and prism facets. These predicted values, which are derived from the best fit to laboratory measurements, allow for the model to produce ice particles with a variety of aspect ratios (as in the ratio of the length of the prism facet to the length of the basal facet).

1.2 Ice Crystal Surface Transitions

Equation 1.1 shows that an ice particle's deposition coefficient will depend on its growth mechanism (M), which in turn depends on the ice surface structure. The KLAH model uses a constant growth mechanism parameter M to predict α, and this assumption is true for crystals with pre-existing facets (such as hexagonal plates and columns). However, the M cannot be constant in all cases, especially for freshly nucleated ice. Laboratory studies, such as those reported by Gonda and Yamazaki (1983), have shown that the facet structure of a frozen droplet will appear over time in a surface transition. Gonda and Yamazaki (1983) produced an intermediate phase as a newly-frozen, spherical particle grew into a hexagonal prism. In the intermediate stage, the particle contained pyramidal facets in addition to the basal and prism facets (Figure 1.7). Unlike the basal and prism facets, the pyramidal facets were apparently comprised of many growth ledges stacked at an angle (like a pyramid) that served as vapor attachment sites. Thus, the pyramidal facets had a high growth efficiency and grew rapidly compared to the other facets, eventually growing themselves out of existence. As a result, the particle growth was first dominated by efficient growth (M that is near 1), to later be dominated by slower 2D nucleation growth for the basal and prism facets (M is near 10).

What Gonda and Yamazaki (1983) showed was that frozen droplets undergo a *surface transition* that substantially affects the growth rate prior to taking on the standard hexagonal prism form. The extent of the impact from this transition on the deposition coefficient has not been explored before, and it may shed light on the disparity in many of the previously discussed laboratory measurements of the deposition coefficient. In fact, there appear to be no prior existing mass growth data sets that reflect the presence of a surface transition, nor is there a model of this type of growth.

1.3 The Current Work

For the work presented, I grew frozen pure water droplets from the vapor inside a levitation diffusion chamber at temperatures near -40 °C. Using the diffusion-kinetics model, I estimated the deposition coefficients for those ice particles by calculating the best fits to the data. I discovered that the model could not duplicate some of the particles' growth rates. Upon further analysis (see Chapter 3), I found that approximating a surface transition by allowing M to vary produced modeled growth that behaved like the data. From this I inferred that surface transitions might have been present on the growing ice particles. Additionally, due to uncertainties on the vapor supersaturation in the experiments, an analysis method was developed to remove the deposition coefficient's dependence on the supersaturation.

This work sheds light on important knowledge missing from the cloud physics literature. It explores the growth of ice particles from the vapor at temperatures where homogeneous freezing is possible and below, which has been rarely been measured previously. Furthermore, it presents a method for determining the extent to which attachment kinetics limit the growth of ice without

the uncertainty inherent in the measured ice supersaturation. With this method, I also show that

the mass growth data indicate the existence of a surface transition. This phenomenon is known to

occur, but is rarely measured and found infrequently in the cloud physics literature. The existence

of surface transitions has not been previously shown with mass growth data from cloud growth

chambers.

Chapter 2

Methods and Analysis

2.1 The Experiment Apparatus

I conducted experiments in the levitation diffusion chamber as described in Harrison et al.

(2016). The top and bottom of the chamber are the surfaces of two parallel copper plates that are

2.57 cm thick and 17.78 cm in diameter. Note that the plates' circular shapes have been trimmed

to be squares with rounded edges (Figure 2.1 from Harrison et al., 2016). A Plexiglas® ring, with

an inner diameter of 10.2 cm, is centered between the plates, separating them by 1.27 cm. The

result is a cylinder with an 8:1 diameter-height ratio, which is large enough to avoid the possibility

of wall effects (Elliot, 1971). Locate on the sides of the plates opposite the Plexiglas® ring are

Plexiglas® cryogen housings. Using two NESLAB ULT-95 baths to circulate the cryogen with

precisely set temperatures, the plate temperatures are controlled independently of each other. The

temperatures of the cryogen and the copper plates are monitored by four Type-T thermocouples,

with one floating in each cryogen housing and one imbedded just beneath the ice-coated surface

of each of the copper plates. The bottom plate is set to a lower temperature than the upper plate to produce a stable environment maintained by thermal and vapor diffusion.

The chamber's top plate is not completely flat like the bottom plate. The top plate has a 1 cm diameter hole at its center to allow for the introduction of water droplets. Additionally, it contains four button electrodes, each 0.95 cm in diameter. The electrodes are attached to the plate such that they form a 3.4 cm diameter circle about the launch opening (Figure 2.1b). Filter paper soaked in high-pressure liquid chromatography (HPLC) water from J.T.Baker® is attached to the upper and lower plates to serve as the vapor source in the experiments. The bottom plate is fully covered with filter plate, but the top plate has filter paper with holes for the launch opening and the electrodes. Vapor produced from ice sublimation on the upper, warmer plate descends to the lower, colder plate via diffusion, resulting in a supersaturated environment. Note that it is possible to measure the supersaturation profile by equilibrating sulfuric acid solution droplets within the chamber, but this method risks contaminating the bottom ice surface, thus altering the vapor field (Harrison et al., 2016).

To levitate ice particles, the chamber utilizes six electrodes in conjunction with the charge on the particle. The electrodes in question are the copper plates and the four button electrodes. The bottom copper plate is given a direct current voltage that produces a vertically positive electric field. This voltage is adjustable and is used to track changes to the levitating particle's mass. The top plate is a grounded electrode. The button electrodes on the top plate receive 180° out-of-phase alternating current voltages. These electrodes serve as a quadrupole, and the resulting AC field produces a saddle point that centers and stabilizes the levitating particle. The particle is charged by exposure to a ~450 V direct current prior to launch.

Once launched, a particle's location and initial size are determined using two digital cameras and a laser. Monochromatic Point Grey® Blackfly® cameras view the interior of the levitation diffusion chamber through windows on opposite sides of the Plexiglas® ring. A 5-mW, 632.8-nm helium–neon laser is directed at the particle, scattering light to both cameras. One camera records the diffraction pattern at nearly 45° from the forward scatter direction. Though the particle remains approximately spherical, the particle's initial size is determined by comparing the diffraction patterns to Mie scatter theory. The other camera views the center of the chamber with both plates visible in the images. Particles in these experiments are too small to see without magnification, but they do reflect enough of the incident laser light to appear as a bright dot to the camera. With the top and bottom of the chamber as references, the particle's height from the bottom of the chamber can be determined, which is necessary to calculate the temperature and ice supersaturation at its location.

2.2 Experiment Process

Prior to experimentation, I apply pure, HPLC water to the filter paper on the copper plates. This ensures a supersaturated environment within most of the levitation diffusion chamber. Recall that the filter paper on the top plate has holes for the button electrodes and the launch opening. It should be noted that this results in a subsaturated area near the top of the chamber (Harrison et al., 2016). However, the experiments presented in this work did not occur in that region. Once wetted, the copper plates cool to approximately -42 °C, freezing the filter paper to the plates. The vapor and thermal fields within the chamber are then allowed to equilibrate for about an hour before any experiments commence.

Experimental runs begin by applying a charge to HPLC water in the droplet launcher. Tapping the launcher causes liquid water to be ejected into the chamber as small (6 – 20 micron) drops. The drops are captured manually by changing the voltage on the bottom plate and the voltage on the button electrodes. A Python^{TM} program developed in the lab adjusts and records the bottom plate's voltage to maintain the particle's vertical location. It is this record of the bottom plate voltage that is used to determine the particle's evolving mass. Simultaneously, I set FlyCapture, the digital camera's user interface, to record the light diffraction patterns. The particle typically freezes within this time.

Throughout the experiment, I may make slight adjustments to the quadrupole in an attempt to stabilize the ice particle, as it might drift from the chamber's center. One such adjustment is to either raise the voltage on the button electrodes or to lower their oscillation frequency. The goal of this is to re-center the particle without disrupting the net vertical component of the electric field. If the particle cannot return to its original horizontal location, the laser may need to be shifted to ensure that the particle is illuminated well enough for the Python^{TM} program to track it.

The experiment ends once the ice particle becomes too unstable to contain. This can occur from either excessive movement or when the particle has gained too much mass during growth. After the experiment, I record the ice thickness on the copper plates with dial calipers to calculate the actual height within the chamber. Additionally, I capture images of a #0-80 threaded rod within the chamber for the purpose of calibrating image pixels to a real distance. After completion of the experiment, the data need to be analyzed, and I turn to that in the following sections.

2.3 Diffusion Chamber Model

Quantifying the growth of an ice particle requires a description of the environment, and one must know the pressure, temperature, and partial pressure of water vapor. During these experiments, I record the pressure and the temperatures of the two copper plates. According to diffusion chamber theory, the temperature within the chamber follows a linear profile, which has been confirmed by prior measurements (Harrison et al., 2016), and makes the process of calculating the temperature at the particle's height straight-forward.

Calculating the vapor pressure is not trivial. Diffusion chamber theory predicts that the vapor field should be parabolic with a maximum vapor density at the vertical center of the chamber. However, this theory assumes that both the top and bottom of the chamber are completely covered in ice. In this diffusion chamber, the ice on the top plate has holes for the button electrodes and launch opening. As a result, the vapor field is non-uniform in those regions. To account for this, I estimate the supersaturation using the diffusion chamber model described in the Appendix of Harrison et al. (2016). This model predicts the vapor and thermal fields with a two-dimensional rectangular diffusion chamber model.

An example of the vapor profile simulated by the model is compared to standard diffusion chamber theory in Figure 2.2. The modeled profile shows a vapor maximum occurring near the bottom third of the chamber. In contrast, diffusion chamber theory states that the vapor maximum should occur at the chamber's midpoint. Also note that the modeled maximum value is expected to be less than the theoretical value. Furthermore, the model produces a subsaturated region near the top of the chamber in response to the "dry" electrodes and launcher opening. The existence of the subsaturated region within this diffusion chamber has been confirmed in previous experiments (Hanson et al., 2016).

2.4 Predicting α with the Diffusion-kinetics Model

Diffusion-kinetics growth can be modeled using the Kinetic Limited Adaptive Habit (KLAH) model of Zhang and Harrington (2014). This model uses parameters determined from the laboratory experiments to model the mass growth of an ice particle. The model does allow for a closed-form solution due to the dependence of the deposition coefficient on the local supersaturation, which further depends on the vapor and thermal diffusion rates. Thus, to calculate the mass of an ice crystal, the KLAH model involves solving the following equations simultaneously (Zhang and Harrington, 2014):

$$\frac{dm}{dt} = 4\pi C(c,a)D(T,p,c,a,\alpha_c,\alpha_a)S_i \tag{2.1}$$

$$D = \left[\frac{RT_\infty}{M_w D_v' e_i(T_\infty)} + \frac{l_s}{M_w k_T' T_\infty}\left(\frac{l_s}{RT_\infty} - 1\right) \right]^{-1} \tag{2.2}$$

$$D_v' = \frac{2}{3} \times \frac{D_v}{\left(\frac{4D_v}{\alpha_c \overline{v_v}}\frac{C}{ac} + \frac{C}{C_\Delta}\right)} + \frac{1}{3} \times \frac{D_v}{\left(\frac{4D_v}{\alpha_a \overline{v_v}}\frac{C}{a^2} + \frac{C}{C_\Delta}\right)} \tag{2.3}$$

$$k_T' = \frac{2}{3} \times \frac{k_T}{\left(\frac{4k_T}{\alpha_{T,a}\rho_a c_p \overline{v_a}}\frac{C}{ac} + \frac{C}{C_\Delta}\right)} + \frac{1}{3} \times \frac{k_T}{\left(\frac{4k_T}{\alpha_{T,c}\rho_a c_p \overline{v_a}}\frac{C}{a^2} + \frac{C}{C_\Delta}\right)} \tag{2.4}$$

In this system of equations, $\frac{dm}{dt}$ is the mass growth rate, C is the particle capacitance as a function of its shape and semi-major axis length, D is the effective diffusivity, S_i is the ambient supersaturation relative to ice, T_∞ is the ambient temperature, p is pressure, c is the prism axis semi-length, a is the basal axis semi-length, α_c is the prism facet deposition coefficient, α_a is the basal facet deposition coefficient, D_v' is the modified vapor diffusivity, and k_T' is the modified thermal diffusivity. The remaining variables are defined in the Appendix. The axis evolution is found by also solving

$$\frac{dc}{da} = \frac{\alpha_c(T, S_i)}{\alpha_a(T, S_i)} \tag{2.5}$$

for the growth of the prism and basal axes, which assumes that ledge growth begins at crystal edges (Nelson and Baker, 1998). The model initializes with the particle's initial radius, ambient temperature, supersaturation, and critical supersaturation. The ice crystals are assumed to be initially spherical, with a radius, r_0. This assumption is justified since the particles are formed from frozen droplets is with an initial radius that is experimentally determined, as discussed above. The values used for the critical supersaturation, S_{crit}, are temperature dependent, have been experimentally determined in the past (Libbrecht, 2003), and can also be determined from our measurements.

Pairing laboratory mass growth data with the KLAH model allows me to estimate the deposition coefficient of each ice particle. This is achieved by simulating the growth of an ice crystal using the KLAH model with different values of α. The results from the KLAH model are then compared to results from the laboratory data via the root mean square mass error to determine the best fit. The model run with the lowest root mean squared is used to select the best-fit value of α. Results presented in Chapter 3 usually use the assumption that the particle is spherical because information on the particle shape is not available, but they remain relatively small, and likely isometric.

2.5 Uncertainty on α

The process of determining the deposition coefficient from laboratory data relies on the data providing an accurate representation of the growth process. Even small errors in experiment conditions, such as supersaturation, can produce large uncertainties on the value of α. If one

desires to know a specific deposition coefficient value, the range of error tolerance must be known.

One can expect high precision to be needed to determine deposition coefficients near unity, as the

growth equation (2.1) loses sensitivity to α if it exceeds about 0.2. This effect can be clearly shown

by simulating the impact of using erroneous mass values in determining the deposition coefficient.

For this analysis, I use an error of

$$\varepsilon = \frac{\sum (m_i - m_t)^2}{\sum m_t^2}, \tag{2.6}$$

where ε is the mass error, m_t is the hypothetical "true" mass of the particle as would be measured

in the diffusion chamber, and m_i is modeled mass. The summations denote an a time integration

as the particle grows. I use the KLAH model to simulate an ice particle growing for 300 seconds

under identical initial conditions of 1000 hPa pressure, -30 °C temperature, 0.1 ice supersaturation,

and 10 μm radius. A "measured" mass timeseries is generated by giving the particle a true

deposition coefficient of α_t. Essentially, α_t is the deposition coefficient that a measurement would

try to extract. The "true" growth timeseries is then compared to the growth of a particle with a

different deposition coefficient, α_i. The error in the modeled mass timeseries is then computed

using Equation 2.6 at each timestep, which provides insight on the accuracy in the mass growth

rate necessary to determine the deposition coefficient within an estimated range.

Results of running these simulations for the known range of α_i and a few select α_t values

are displayed in Figure 2.3. The x-axis represents the predicted deposition coefficient, the y-axis

corresponds to the mass error at the end of the simulation, and each curve is for a different true

deposition coefficient. Unsurprisingly, the error minimizes when $\alpha_i = \alpha_t$. Note that any value

of α_i below a given error threshold cannot be distinguished from α_t. For example, if a mass error

of 5% can be tolerated, the curve for $\alpha_t = 0.01$ has $0.006 \leq \alpha_i \leq 0.015$. In such a scenario, while

the true deposition coefficient is 0.01, one may determine the deposition coefficient to be anywhere between 0.006 and 0.015 with equal certainty. Thus, if mass growth errors are small (i.e. $5 - 10\%$), relatively low values of the deposition coefficient can be accurately determined. Figure 2.3 also reveals that, as α approaches unity, it becomes increasingly difficult to distinguish among other deposition coefficients. It will become clear in later sections that this effect is critical, causing growth curves with α greater than about 0.05 to be nearly identical and making it nearly impossible to conclude if growth is limited by attachment kinetics.

The difficultly in distinguishing deposition coefficient values greater than about 0.05 can be more clearly shown through the following analysis: allow the points at which the α_t curves cross a chosen error threshold (5% in Figure 2.3) to be α_1 and α_2, with α_1 the lesser value and α_2 the greater value. If the curve only crosses the threshold once, and it ascends to the right, then α_1 is taken as the minimum α_i value used. Conversely, if the curve crosses only once, and descends tot the right at that point, then α_2 is unity. Now let

$$\Delta\alpha = \alpha_2 - \alpha_1, \tag{2.7}$$

where $\Delta\alpha$ is the range of α_i below the chosen mass error threshold. For example, recall that the $\alpha_t = 0.01$ curve on Figure 2.2 crosses the $\varepsilon = 5\%$ at 0.006 and 0.015. In this case $\alpha_1 = 0.006$ and $\alpha_2 = 0.015$, resulting in $\Delta\alpha = 0.009$. If one compares many values of α_t to $\Delta\alpha$ for various error thresholds (Figure 2.4), an intriguing pattern emerges. For small α_t, $\Delta\alpha$ is near zero, but larger α_t have $\Delta\alpha$ rapidly ascending towards unity, indicating that determining α becomes impossible. An error of 5% in the mass growth rate causes $\Delta\alpha$ rise abruptly between 0.03 and 0.04.

The jump in $\Delta\alpha$ toward unity has significance. It indicates that if the true deposition coefficient is above some critical value, then a small error or uncertainty in the mass data makes it

nearly impossible determine α accurately. If a particle has a true deposition coefficient of $\alpha_t = 0.05$, and there is a mass error in the data of $\varepsilon = 5\%$, then $\Delta\alpha = 0.97$. As Figure 2.3 reveals, this would mean that α lies between $\alpha_1 \approx 0.02$ and $\alpha_2 \approx 0.99$. That range in deposition coefficients covers nearly all of kinetics-limited growth and diffusion-limited growth. As a result, there is no definitive way to determine this particle's growth mode, and the reported deposition coefficient may be up to 0.95 larger than its true value. The implications of a $\Delta\alpha$ close to unity are unsettling, as it means that any deposition coefficient determined from growth data may be flawed and far from the true value if that value is above about 0.04. This may in part explain the divide between high and low values of the deposition coefficient found in past studies, as discussed in Section 1.1. Thus, uncertainties in laboratory data can have a substantial impact on the reported deposition coefficient, which casts doubt onto past, present, and future measurements.

Note that the value of α_t at which the jump in $\Delta\alpha$ occurs depends on the surrounding environment, though the strongest dependence is on temperature and pressure. Using the above process, I calculated the values of α_t when $\Delta\alpha$ reached 0.1 (the beginning of the jump shown in Figure 2.4) and 0.5 (the middle of the jump shown in Figure 2.4). I focused the calculations on a mass error of 10%, as this is likely the highest expected precision from most cloud diffusion chambers. I ran simulations for temperatures between 0 and -70 °C, with pressures of 1000 hPa and 100 hPa. Figure 2.5 shows that at 1000 hPa and temperatures above about -45 °C, the jump in $\Delta\alpha$ occurs when α_t is on the order of 0.01 to 0.02. However, the jump appears for much smaller α_t values at lower temperatures. As a result, it would be nearly impossible to determine the relatively high values of the deposition coefficient for ice particles growing at temperature less than -45 °C and 1000 hPa, if the mass data had a 10% error. This is problematic for any future experiments that attempt to study the deposition coefficient at low temperatures found in cirrus

clouds, which fall well below -45 °C. Fortunately, at lower pressure the $\Delta\alpha$ jump happens at larger values of α_t. Lower pressure provides better resolution at higher α_t values. If the pressure is 100 hPa, then about -65 °C becomes the temperature at which α_t greater than about 0.001 cannot be resolved. Since cirrus clouds may form above the 200 hPa pressure level and at temperatures below -40 °C, having better resolution on α_t in experiments under such conditions is preferred.

2.6 Power-law Analysis

Relatively accurate estimates of the supersaturation within the chamber and the initial size of the ice particle are required to fit the measured mass ratio timeseries with a model. It is difficult to achieve the 5% minimum absolute error that the above analysis suggests is necessary to accurately determine the deposition coefficient in the range 0.05 to 1. To address this challenge, I conducted a form of scale analysis on the data similar to that of Harrison et al. (2016), which removes the dependence on supersaturation. This analysis generated a growth power law that allows me to easily compare the data with model output without the influence supersaturation uncertainty. This analysis method does not provide direct information on the deposition coefficient, though it does give insight on whether growth is limited by surface attachment kinetics.

Following Swanson et al. (1999), Equation 2.1 is normalized by its initial value. Due to the supersaturation, temperature, and pressure being constants, one finds for diffusion-limited growth that

$$\frac{\dot{m}}{\dot{m}_0} = \frac{r}{r_0}, \qquad (2.8a)$$

where the mass rate of change has been written in Newtonian notation for convenience, r is the radius of an equivalent volume sphere, and the zero subscripts denote initial values. Additionally, this same ratio for growth that is entirely kinetics-limited becomes

$$\frac{\dot{m}}{\dot{m}_0} = \frac{r^2}{r_0^2}. \qquad (2.8b)$$

This ratio goes as the radius squared due to kinetics-limited growth's dependence on the particle surface area. Diffusion-kinetics limited growth has a similar power law dependence that lies between pure diffusion- and kinetics-limited growth. In such a regime, the effective diffusivity, D in Equation 2.1, tends to have a size-dependent power law (as shown by the solid curves in Figure 3.8b). I can then write the effective diffusivity as

$$D = D_0 \left(\frac{r}{r_0}\right)^{1-n}, \qquad (2.9)$$

with D_0 as the effective diffusivity at the initial particle size, and n is a power typically between 0 and 1. Harrison et al. (2016) showed that the deposition coefficient tends to decrease with increasing size, which leads to a similar power law

$$\alpha = \alpha_0 \left(\frac{r_0}{r}\right)^{n}, \qquad (2.10)$$

where α_0 is the deposition coefficient at the initial size. Substituting Equation 2.9 into Equation 2.1, and taking its ratio as in Equation 2.8, shows that for diffusion-kinetics limited growth

$$\frac{\dot{m}}{\dot{m}_0} = \left(\frac{r}{r_0}\right)^{2-n}. \qquad (2.11)$$

We now see that an *n* of zero applies to kinetics-limited growth and *n* of unity applies to diffusion-limited growth. Experiments with the levitation diffusion chamber produce direct measurements of mass ratios. It is therefore useful to rewrite Equation 2.11 in terms of mass. Since the radius of a sphere is proportional to the cubic root of its mass,

$$r \propto m^{1/3},$$

(2.12)

with *m* as the mass, Equation 2.11 can be rewritten as

$$\frac{\dot{m}}{\dot{m}_0} = \left(\frac{m}{m_0}\right)^{(2-n)/3},$$

(2.13)

where m_0 is the initial particle mass. Taking the natural logarithm of both sides of 2.13 gives

$$\ln\frac{\dot{m}}{\dot{m}_0} = \frac{2-n}{3}\ln\frac{m}{m_0}.$$

(2.14)

Dividing both sides of 2.14 by the natural logarithm of the normalized particle mass results in

$$\frac{\ln\left(\frac{\dot{m}}{\dot{m}_0}\right)}{\ln\left(\frac{m}{m_0}\right)} = \frac{2-n}{3} = P,$$

(2.15)

where *P* is the derived particle mass growth power law. Equation 2.15 is independent of both the supersaturation and the initial particle radius, which are the two largest sources of uncertainty in the chamber measurements. Also, note that the left-hand side of 2.15 can be computed directly from the mass data without any model interpretation.

One would expect the growth power law *P* to range from 1/3 for diffusion-limited growth to 2/3 for kinetics-limited growth. Chapter 3 will explore the results of this analysis when applied

to the data, the model, and a slightly modified version of the model that includes a variable-M growth mechanism.

2.7 Scale Analysis to Determine α

In Section 2.5, it was shown that relatively small uncertainty in measured growth data strongly propagates to the deposition coefficient prediction. Furthermore, the ice supersaturation in the experiments described in Chapter 3 is estimated by a model rather than measured. Though the model serves as a reasonable proxy for the supersaturation, it can produce errors on the order of 10%, perhaps more (Harrison et al., 2016). To avoid errors in the supersaturation and the initial size, a new analysis method is developed in this work to fit the model output on the effective diffusivity, which is then used to determine the deposition coefficient. Through this analysis, the ice particle growth rate is normalized by its mean value and written in terms of mass ratios, which eliminates the supersaturation and initial size dependence from the growth equation. The analysis method presented in Section 2.6 could be used, but there retains a significant source of uncertainty in its dependence on the particle's initial mass growth rate. Conversely, the mean growth rate, as used below, is significantly more robust as it is computed over the entire timeseries.

In this analysis method, I return to a modified version of Equation 2.1:

$$\dot{m} = 4\pi r D S_i. \tag{2.16}$$

Again, $\dot{m}$ is the mass growth rate, r is the volume-equivalent sphere radius, D is the effective diffusivity and S_i is the ice supersaturation. Converting r into mass, since mass ratios are measured, gives

$$\dot{m} = 4\pi \left[\frac{3}{4\pi\rho_i}m\right]^{1/3} DS_i, \tag{2.17}$$

where ρ_i is the density of ice. I then define the mass growth rate ratio as

$$\dot{m}_r \equiv \frac{\dot{m}}{m_0} \tag{2.18}$$

and the mass ratio is

$$m_r \equiv \frac{m}{m_0}, \tag{2.19}$$

where m_0 is the initial ice particle mass. Normalizing Equation 2.17 by the initial mass then gives

$$\dot{m}_r = \kappa m_r^{1/3} DS_i, \tag{2.20}$$

where κ is a constant at

$$\kappa = \left[\frac{48\pi^2}{m_0^2\rho_i}\right]^{\frac{1}{3}}. \tag{2.21}$$

Equation 2.20 applies to general diffusion-kinetics growth. To draw meaning from it, one must compare it to the kinetic and diffusion limits of growth. Following Section 2.6, the kinetics and diffusion limits of the mass growth rate ratio are, respectively,

$$\dot{m}_r = r_0 \kappa m_r^{2/3} \alpha \frac{1}{4}\overline{v_v}\rho_{eq}S_{local} \tag{2.22}$$

and

$$\dot{m}_r = \kappa m_r^{1/3} D_0 S_i, \tag{2.23}$$

where r_0 is the initial particle radius, $\overline{v_v}$ is the mean speed of a vapor molecule, ρ_{eq} is the equilibrium vapor density, S_{local} is the supersaturation at the particle surface, and D_0 is the diffusivity at the

initial size. Note that Equation 2.22, the kinetics-limited growth equation, follow the standard Hertz-Knudsen formulation (see Libbrecht, 2003) by multiplying the crystal surface area ($4\pi r^2$) by the deposition coefficient and the kinetic theory vapor flux. Keep in mind that the difference in exponents of the mass ratio originates from Equation 2.8 and that the exact values of κ, r_0, $\overline{v_v}$, ρ_{eq}, S_{local}, D_0, and S_i are not needed, as they are constant and will drop out of the analysis. The scale analysis below assumes that pure kinetics-limited growth has a constant α with size, though this approximation will be shown to not always be justifiable. Recall that the diffusion chamber environment is highly stable; thus the supersaturation and temperature do not change with time.

Beginning with the kinetics limit as a convenient reference growth rate, taking the mean of Equation 2.22 gives

$$\overline{\dot{m}_r} = r_0 \kappa \alpha \frac{1}{4} \overline{v_v} \rho_{eq} S_{local} \overline{m_r^{2/3}}. \tag{2.24}$$

Normalizing by the instantaneous growth rate ratio (Equation 2.22) by its mean (Equation 2.24), I find that

$$\frac{\dot{m}_r}{\overline{\dot{m}_r}} = \frac{m_r^{2/3}}{\overline{m_r^{2/3}}}. \tag{2.25}$$

Realize that these steps are similar to the procedure in Section 2.6. Both methods remove the supersaturation and temperature dependence since everything else is given in terms of mass ratios. The main difference between the methods is that the one discussed here utilizes the robustness of the mean growth rate instead of the uncertain initial growth rate.

If I define the scaled mass growth rate ratio as

$$\dot{m}_s \equiv \frac{\dot{m}_r}{\overline{\dot{m}_r}} \overline{m_r^{2/3}}, \tag{2.26}$$

then I may use the natural logarithm to write Equation 2.25 as

$$\ln \dot{m}_s = \frac{2}{3} \ln m_r. \tag{2.27}$$

Interestingly, both sides of Equation 2.27 can be derived directly from the laboratory data. The sole variable on the right-hand side is the mass ratio, which is very precisely known. The left-hand side depends on the mean of the mass ratio, the instantaneous growth rate ratio, and the mean growth rate ratio. Both averaged values are accurately known, leaving the instantaneous growth rate ratio as the main source of error.

To compare the laboratory determined growth rates, I also need the scaled mass growth rate of the diffusion limit. Following a similar procedure, and rewriting Equation 2.23 with a scaled mass growth rate ratio gives

$$\ln \dot{m}_s = \ln \left[\frac{\overline{m_r^{2/3}}}{\overline{m_r^{1/3}}} \right] + \frac{1}{3} \ln m_r \tag{2.28}$$

for the diffusion limit. Again, for Equations 2.27 and 2.28, all of the mass related variables are derived directly from the mass ratio data.

Calculating the scaled mass growth rate ratio for the diffusion-kinetics case is more challenging, since the diffusivity varies with size, even if the deposition coefficient is constant. As a result, the mean of the mass growth rate ratio becomes

$$\overline{\dot{m}_r} = \kappa S_i \overline{m_r^{1/3} D} = \kappa S_i \overline{m_r^{1/3}} \overline{D_r}, \tag{2.29}$$

where

$$\overline{D_r} = \frac{\sum m_r^{1/3} D}{\sum m_r^{1/3}} \tag{2.30}$$

is the radius-weighted average diffusivity. Dividing Equation 2.20 by Equation 2.29 and using the same natural logarithm manipulation as in the diffusion and kinetics cases results in

$$\ln \dot{m}_s = \ln \left[\frac{\overline{m_r^{2/3}}}{\overline{m_r^{1/3}}} \right] + \frac{1}{3} \ln m_r + \ln \left[\frac{D}{\overline{\overline{D_r}}} \right].$$

Again, all or the mass-related values can be computed directly from the data; uncertain quantities, such as the supersaturation and the initial size, have been removed from the analysis. The only remaining unknown values are the effective diffusivity and its mean, as they appear in Equation 2.31, which weakly depend on temperature and strongly on the deposition coefficient and size (Equation 2.2). All of the other variables in Equation 2.31 can be determined from the mass data. Since the temperature is constant, the only parameter that can be adjusted to fit the data is the deposition coefficient. The diffusivity-terms are, therefore, determined by using the KLAH model to find the best fit to the data. The deposition coefficient can then be extracted from the diffusivity without reference to the supersaturation or the initial size. In fact, this method can be used to estimate the supersaturation from Equation 2.29 as

$$S_i = \frac{\overline{\dot{m}_r}}{\kappa \overline{m_r^{1/3} \overline{D_r}}}.$$

(2.32)

This supersaturation and the one derived from the diffusion chamber model are used together as the error range on the supersaturation.

To summarize, the scaling method of computing the mass growth rates proposed above removes the supersaturation dependence from the model fitting process. The scaling method can estimate the deposition coefficient more reliably than the traditional method of fitting to the mass timeseries due to the deposition coefficient being the only unknown in the scaling method. Additionally, a new method of estimating the supersaturation emerges from this analysis. Note that the main equations derived from this analysis are listed in Table 2.1.

Table 2.1 Final scale analysis equations

Listed are the main equations pertinent to the mass growth rate scaling analysis. The right-hand side of the first three equations are calculated from the data, and the fourth is derived from a best-fit simulation.	
Data	$$\ln \dot{m}_s = \ln \left[\frac{\dot{m}_r}{\overline{\dot{m}_r}} \overline{m_r^{2/3}} \right]$$
Kinetic limit	$$\ln \dot{m}_s = \frac{2}{3} \ln m_r$$
Diffusion limit	$$\ln \dot{m}_s = \ln \left[\frac{\overline{m_r^{2/3}}}{\overline{m_r^{1/3}}} \right] + \frac{1}{3} \ln m_r$$
Diffusion-kinetic	$$\ln \dot{m}_s = \ln \left[\frac{\overline{m_r^{2/3}}}{\overline{m_r^{1/3}}} \right] + \frac{1}{3} \ln m_r + \ln \left[\frac{D}{\overline{D_r}} \right]$$

Chapter 3

Results and Discussion

3.1 Initial Laboratory Data and Preliminary Analysis

The theoretical analysis methods proposed in Chapter 2 will be used in the laboratory data analysis presented in this chapter. Prior to utilizing those analysis methods, I display the raw data as they are. Figure 3.1(a-c) shows the mass timeseries data for each of ten successful experiments. Most of the particles grew for less than 2200 s (0.56 hr), with the sole exception of particle #5, which grew for over 18000 s (5 hr). (That particle will be explored in more detail later in this chapter.) Additionally, particles typically grew to no more than ten times their initial masses, with four exceptions that grew beyond fifteen times the initial mass.

A few features of interest that are immediately apparent in Figure 3.1 are the following: First, as previously mentioned, particle #5 grew for an exceptionally long, 5-hr period (Figure 3.1c). Furthermore, its mass growth rate is nearly constant in time, which is not possible without an effective diffusivity that decreases with size, as I will elaborate upon below. Other striking features are the rapid growth rates of particles #8, #9, and #10 (Figure 3.1b). Another noteworthy element is similarity between the growth of particle #2 and #3 as their timeseries nearly overlap.

Interesting, qualitative statements can be made about the data in Figure 3.1, but they have little meaning in the absence of the conditions that the particles grew under. This information, listed in Table 3.1, is crucial to the analysis process. As discussed in Chapter 2, the initial radius is determined by analyzing the diffraction fringe patterns resulting from Mie scattering. The uncertainty on this value is the standard deviation from the mean radius calculated from images

taken over ten seconds. The pressure measurement is taken from a barometer in the laboratory.

The copper plate temperatures are measured by Type-T thermocouples that have a 0.1 °C

resolution. The temperature at the particle location is calculated from diffusion theory that

produces a linear temperature profile between the two plates, which is relatively accurate

(Harrison et al., 2016). The uncertainty in the particle temperature, when accounting for

uncertainty on the plate temperatures and the particle tracking, is ± 0.17 – 0.20 °C in all cases.

Since the temperature measurements have a single decimal, I estimate the temperature

uncertainty to always be ± 0.2 °C. Note that the particle location uncertainty is ± 0.1 mm,

according to Harrison (2013).

Table 3.1 Environment conditions for each particle

Listed are the environment parameters necessary to describe and analyze the particle growth. Particle numbers correspond to the date (YYYYMMDD) and time (hhmmss) that growth began. The parenthetical numbers are used for short-hand reference within the text. The copper plate temperatures all have an uncertainty of ± 0.1 °C. Particle temperatures have an uncertainty of ± 0.2 °C.

Particle #	Initial radius (μm)	Pressure (hPa)	Top plate temp. (°C)	Bottom plate temp. (°C)	Temp. at particle (°C)
20160614-132805 (1)	15.05 ± 0.43	978.	-36.3	-46.9	-42.2
20160614-143412 (2)	10.60 ± 0.20	978.	-36.1	-46.9	-42.1
20160614-154240 (3)	10.82 ± 0.42	978.	-36.4	-46.9	-42.2
20160628-144717 (4)	9.25 ± 0.32	973.	-37.2	-46.4	-42.4
20160628-152650 (5)	21.55 ± 0.35	973.	-37.3	-46.3	-42.4
20160726-112828 (6)	17.50 ± 0.88	977.	-34.6	-45.3	-40.8
20160726-124528 (7)	12.41 ± 0.20	976.	-34.5	-45.4	-41.1
20160801-142906 (8)	10.55 ± 0.16	979.	-34.6	-45.2	-40.2
20160809-130942 (9)	8.65 ± 0.39	983.	-37.8	-48.1	-43.4
20160809-135510 (10)	9.82 ± 0.38	983.	-37.8	-48.1	-43.4

Another feature in the raw data is a low frequency oscillation appears in the mass timeseries. While the oscillations are small in the raw data (Figure 3.2a), they have a pronounced appearance in the mass derivative (Figure 3.2b). The mass derivative shows the low frequency oscillation superimposed on the high frequency noise associated with the small voltage changes that stabilized the particle during levitation. The low frequency oscillation is presumably

generated as an artifact of the particle levitation software. This assertion is based on evidence from the work of Harrison (2013). The software used by Harrison (2013) only adjusted the particle's location upwards. As a result, the data have a step-like pattern, leading to high frequency features in the mass derivative that are easily removed with a low pass filter. On the other hand, the current software was written to be more general, allowing the particle to move both upwards and downwards. (Downward movement is necessary in the event of particle sublimation (Hanson et al., 2016)). The new software "over-corrects" when moving the particle either upwards or downwards, causing a quasi-regular oscillation to appear in the data. A low pass filter can partially remove some of the oscillation, as was done in both this work and that of Harrison (2013), but it is not always successful. Much of the analysis presented below requires the particle growth rate, and these oscillations amplify the calculated growth rates (Figure 3.2b).

Besides using a low pass filter on the data, I follow Magee et al. (2006) and analyze cubic spline fits to the data, which are shown as dashed curves in Figures 3.1 and 3.2. The coefficients for each fit are listed in Table 3.2. Note that in all cases $C_0 \approx 1$. This is due to the normalization of the mass by its initial value (at time $t = 0$). Additionally, the coefficients quantify the earlier qualitative observations regarding patterns of particle growth. For example, the second and third order terms for particle #5 are two and three orders of magnitude smaller than most of those of the other particles. Thus, for particle #5, $m_r \cong C_0 + C_1 t$, is nearly a linear function. The rapid growth of the last three particles also becomes clear, as their third order terms are one or two orders of magnitude great than what is measured for most other particles. Likewise, the similarity between particles #2 and #3 is quantified by all of their coefficients being within 10% of each other, excluding the third order coefficients. Nevertheless, the cubic fits accurately capture all of the

data, and I use both the cubic fits and the data smoothed by a low pass filter in calculating the

growth rates.

Table 2.2 Data cubic fit coefficients

Cubic fit coefficients for each dataset with $m_r = C_0 + C_1t + C_2t^2 + C_3t^3$, where m_r is the ratio of the particle mass to its initial value, and t is the time of growth.				
Particle #	C_0	C_1 ($\times 10^{-3}$)	C_2 ($\times 10^{-6}$)	C_3 ($\times 10^{-10}$)
20160614-132805 (1)	0.9553	3.366	1.846	-2.138
20160614-143412 (2)	0.9577	6.899	3.081	4.250
20160614-154240 (3)	1.017	6.231	3.015	-0.8887
20160628-144717 (4)	1.005	2.660	0.7702	-2.032
20160628-152650 (5)	0.9137	0.7133	0.02477	-0.006254
20160726-112828 (6)	0.9918	5.625	1.168	6.770
20160726-124528 (7)	0.9549	3.519	3.642	14.87
20160801-142906 (8)	1.042	7.858	6.115	-4.037
20160809-130942 (9)	0.9720	12.88	6.826	153.8
20160809-135510 (10)	1.096	7.602	8.777	13.06

The final preliminary analysis is to run the diffusion chamber model to estimate the ice

supersaturation at the particle location. This requires the tracked location of the particle, the

temperatures of the copper plates, and the thickness of the ice-covered filter paper. The particle

locations and plate temperatures on a given day were always within the uncertainty range of each

other, and so I assume the same ice supersaturation for all particles grown on the same day. The

model results, listed in Table 3.3, have an uncertainty range dependent upon the uncertainty in the

thickness of the ice on both plates and the uncertainty in the size of the "dry" region and the

chamber's top (see Chapter 2; Harrison et al., 2016, Appendix A). These supersaturations will be used mainly for fitting the mass growth timeseries data with the KLAH model. Recall that the supersaturation will not be needed for the data analysis using two the methods described in Sections 2.6 and 2.7 (power law analysis and scaling analysis).

Table 3.3 Diffusion chamber model supersaturations

Modeled ice supersaturations for each day of particle growth.	
Day	S_i **(%)**
20160614	15.4 ± 1.3
20160628	11.0 ± 0.9
20160726	15.7 ± 1.2
20160801	14.9 ± 1.2
20160809	14.6 ± 1.1

3.2 Linear Mass Growth and Ice Surface Transitions

The previous section highlighted the time-linearity of the mass growth of particle #5. This is most intriguing, as the mass growth rate is constant in time, yet according to Equation 2.1, the ice particle's mass growth rate should increase as its radius (capacitance) increases. As Figure 3.8c shows, the effective diffusivity (D) increases with size when the deposition coefficient is predicted with the standard diffusion-kinetics theory. The data from particle #5 imply that both C and D cannot increase with size, as the mass growth rate would also rise, as should occur in classic, faceted growth. Furthermore, these data cannot be rejected, as there were no known defects with the chamber, and the particle growth was highly stable over 5 hours.

If I can no longer assume that *C* and *D* both increase with size, then the ice crystal growth theory must not be general enough and requires modification. It may be that the growth of a particle directly after freezing cannot be accurately modeled by either the capacitance model or faceted growth theory. The capacitance *C* is proportional to the particle's semi-axis length, and depends only on the particle's shape; thus, it must increase with the particle size (Lamb and Verlinde, 2011). However, according to faceted growth theory, the effective diffusivity will also rise with size. Therefore, in the case of particle #5, the effective diffusivity *D* must decrease with increasing size, which can only be done through the deposition coefficient. The size dependence of the effective diffusivity appears both explicitly and implicitly through the deposition coefficient. If the deposition coefficient substantially decreases as the particle grows, *D* would also decrease.

The simplest explanation of a decreasing deposition coefficient, and effective diffusivity, is the presence of a surface transition. A surface transition would cause the growth mechanism *M* to change. For example, Gonda and Yamazaki (1983) showed that frozen water droplets transform into hexagonal prisms through an intermediate stage of rapid growth. During the formation of a single crystal, the prism, basal, and pyramidal facets form shortly after droplet freezing. Recall from Section 1.2 that vicinal faces with numerous ledges comprise the pyramidal facets, and they therefore experience highly efficient growth. In contrast, the basal and prism facets grow more slowly, representative of 2D nucleation. The rapidly growing pyramidal facets quickly grow themselves out, leaving only the slowly growing basal and prism facets. The expected result is a transition that causes a rapid decline in particle mass growth efficiency, and therefore the deposition coefficient.

The measurements of Gonda and Yamazaki (1983) offer a plausible mechanism by which the deposition coefficient rapidly declines for single crystal ice. However, it is possible that my

droplets, when frozen, produce polycrystalline ice, but a process similar to that shown by Gonda and Yamazaki (1983) may occur. In polycrystalline freezing, crystallographically dissimilar facets form grain boundaries between themselves. Grain boundaries are a source of dislocations that propagate away from the source, and therefore produce efficient growth (Figure 3.3 from Pedersen et al., 2011). Initially, grain boundaries are openly exposed to the vapor field, which supplies them with vapor. As the crystal grows, emerging facets expand away from the grain boundaries, as would occur during the formation and growth of a bullet rosette. The grain boundaries are left isolated in the interior, away from the water vapor field with only the inefficiently growing facets left directly exposed to the vapor. I hypothesize that my frozen droplets may behave similarly, and I therefore expect the growth mechanism to change from dislocation to 2D nucleation growth over time. Quantitatively, this growth transition can be represented by increasing M from 1 to 10 in the parametric model of the deposition coefficient. A consequence of increasing M is a decrease in α and a decreasing D, which can produce linear particle mass growth. The impacts of simulating particle growth with a variable M will be explored later in this chapter.

3.3 KLAH Model Timeseries Fits

Using the KLAH model to fit the measured ice particle mass growth timeseries is the first method I utilize to determine the deposition coefficient, which is the typical approach taken in the literature (e.g. Magee et al., 2006; Skrotzki et al., 2013). As described before, the KLAH model uses the environmental parameters listed in Tables 3.1 and 3.3 to produce simulations that closely resemble the data. The deposition coefficients and critical supersaturations determined by the KLAH model are listed in Table 3.4. These results assume that the particles are isometric and are

growing by ledge nucleation ($M = 10$), though the crystals may have grown by dislocations ($M = 1$), stacking faults ($2 \leq M \leq 5$), or some other mechanism. In some cases, simulations of columnar growth produce smaller errors, but these are not significant enough to change the qualitative description of the fit. Thus, I model isometric particles to fit the data, since the actual shapes are unknown and non-spherical fits do little to reduce the fit errors.

Table 3.4 Mass ratio timeseries fit results

Results of the KLAH model fits assuming isometric particles with $M = 10$. Four particles are fit well with a minimum absolute error less than 5%, three are fit moderately well with the error between 5 and 15%, and three are fit poorly with errors exceeding 20%.

Particle #	α	S_{crit} (%)	Minimum absolute error (%)
20160614-132805 (1)	0.76	0.11	9.12
20160614-143412 (2)	0.12	0.96	0.645
20160614-154240 (3)	0.078	1.6	1.10
20160628-144717 (4)	0.0059	10.	2.28
20160628-152650 (5)	0.0027	10.	6.43
20160726-112828 (6)	0.85	0.076	53.7
20160726-124528 (7)	0.032	3.7	8.86
20160801-142906 (8)	0.065	1.6	1.65
20160809-130942 (9)	0.92	0.16	23.3
20160809-135510 (10)	0.97	0.79	42.1

 While the KLAH model produced accurate fits for ice formed from heterogeneously nucleated particles (Harrison et al., 2016), the results for homogeneously frozen droplets are mixed. For example, the data for particle #2 are modeled with a minimum absolute error of less than 1%. Conversely, the model's minimum absolute error for particle #6 is over 50%. If I set qualitative boundaries for accuracy of the model fits to the data as "well" (minimum absolute error:

0 – 5%), "moderately well" (minimum absolute error: 5 – 20%), and "poorly" (minimum absolute

error: > 20%), there is an almost even distribution amongst the categories.

Particle #8 is an example of one of the particles that was fit accurately by the KLAH model

(Figure 3.4). The model fit intersects the data points and has a low overall error. On the other

hand, particle #10 was impossible to fit with the model (Figure 3.5) even though a deposition

coefficient of nearly unity (highly efficient growth) and a critical supersaturation less than 1%

(readily producing attachment sites) were used. Particle #10's growth rate is very large, indicating

that either the supersaturation estimates are too low or that the particle quickly became non-

isometric. Alternatively, its growth may have become electrically enhanced. In such a case, the

ice particle would have enough electrons on its surface to attract vapor molecules

electrodynamically. Such an occurrence would have led to the particle experiencing an

exponential mass growth rate, so this does not appear to be a likely explanation for the large, but

not exponential, growth rate.

Within the spectrum of well and poorly modeled timeseries is the model fit to the measured

mass growth of particle #5 (Figure 3.6). As I discussed in the previous section, the current

theoretical models cannot produce a linear mass timeseries, as current theory predicts that the

particle's growth rate must increase with size. No combination of parameters (i.e. temperature,

supersaturation, initial size, growth time, or growth mechanism parameter) will produce linear

mass growth with the classical ice crystal growth theory.

The KLAH model fit of each mass timeseries demonstrate nearly diffusion-limited growth,

as the deposition coefficient approaches unity, with the only exceptions being the two from

20160628 (particle #4 and #5). Furthermore, the KLAH model suggests that those particles should

have incredibly low critical supersaturations, with some less than 1%. This is in contrast to S_{crit}

values found in other experiments conducted at similar temperatures, which range from 5 – 20% at -40 °C (see Figure 1.3).

The results from these fits to the particle mass timeseries are not robust. They are highly sensitive to the supersaturation in the levitation diffusion chamber, and as previously stated, the supersaturation is uncertain. Additionally, the poor fits between the model and the data provide little confidence in the α and S_{crit} values produced. For these reasons, the data must be analyzed with a method that removes the dependence on S_i and can explain the growth patterns (i.e., linear, rapid) that the model does capture.

The two analysis methods described in Chapter 2 serve as alternative approaches for fitting the data. Both analyses still utilize the KLAH model, but they remove the supersaturation dependence and expose more complex growth features (e.g., possible surface transitions) hidden within the timeseries data. Here, I first use the power law analysis from Section 2.6, followed by the scaling analysis from Section 2.7.

3.4 Power Law Results

The first analysis technique I will use is the power law analysis on the normalized particle growth rate discussed in Section 2.6. Section 2.6 showed that $P = (2 - n) / 3$, where $n = 0$ ($P = 2/3$) for kinetics-limited growth, $n = 1$ ($P = 1/3$) for diffusion-limited growth, and n should be between 0 and 1 ($1/3 \leq P \leq 2/3$) for diffusion-kinetics growth. This method eliminates the supersaturation dependence in quantitatively determining an ice particle growth mode.

Interestingly, the power laws determined for cubic spline fits of the data are outside of the expected $1/3 \leq P \leq 2/3$ range for about 80% of the grown particles (Figure 3.7, Table 3.5). Particles

#2, 3, 4, 5, and 9 all have power law exponents less than 1/3 for the entirety of their growth, and

particles #6, 8, and 10 have exponents less than 1/3 for at least the initial stages of growth. Only

particles #1 and 7 follow the expected $1/3 \leq P \leq 2/3$ trend.

Table 3.5 Power law results

Average power law exponents for the cubic fits of each dataset. $P_{ave} < 1/3$ for all particles excluding #1, 7, and 10.	
Particle #	P_{ave}
20160614-132805 (1)	0.362
20160614-143412 (2)	0.236
20160614-154240 (3)	0.248
20160628-144717 (4)	0.221
20160628-152650 (5)	0.146
20160726-112828 (6)	0.277
20160726-124528 (7)	0.643
20160801-142906 (8)	0.314
20160809-130942 (9)	0.222
20160809-135510 (10)	0.428

These results imply that n is greater than 1 in many cases. If the deposition coefficient

follows a power law as suggested by Equation 2.10, $\alpha = \alpha_0 \, (r_0 \, / \, r)^n$, then it should decrease faster

when $n > 1$ than the slower decline of the classic kinetics limit for faceted growth. These results

suggest that the deposition coefficient deceases faster than classical faceted growth theory predicts.

As discussed in Section 3.2, the only known process that could cause a rapid decrease in α is a

surface transition in which the growth mechanism parameter M increases. Therefore, I hypothesize

that the occurrence of surface transitions can cause the power law exponents to exist outside of the range presented by classical theory.

To examine the plausibility of this hypothesis, I test the idea in idealized simulations using the KLAH model across a range of ice supersaturations with both a constant M (classical faceted ice growth theory) and a variable M (hypothesized surface transition). In each case, I model particle radius growth across $20 - 100$ µm at $T = -40$ °C and $p = 1000$ hPa with $S_{crit} = 10\%$. For constant M, I use $M = 10$, and for variable M, I assume a simple power-law form of the transition,

$$M = 1 + 9 \left[\frac{\min(r, r_f) - r_0}{r_f - r_0} \right]^{3/4}, \tag{3.1}$$

where r is the particle radius, r_0 is the initial radius, and r_f is the final radius. As a result, M transitions from 1 to 10 as the particle's size increase. Simulations were done with supersaturations of 1, 5, 10, and 20%.

The KLAH simulations that assume classical, faceted growth with constant M behave as expected (Figure 3.8a). P stays within the 1/3 to 2/3 range for every S_i. Furthermore, $P \approx 2/3$ at low ice supersaturations ($S_i = 1\%$) as the growth is near the kinetics limit, while $P \approx 1/3$ at high ice supersaturations ($S_i = 20\%$) as the growth approaches the diffusion limit. The simulations of a surface transition with variable M, on the other hand, all have $P < 1/3$, regardless of the supersaturation. Moreover, unlike the classical model where M is constant, P decreases with decreasing S_i. For low supersaturations, P may become negative. This indicates that the current model can simulate growth with values of $P < 1/3$, but only if it includes a growth mode change from one of efficient growth ($M = 1$) to another of inefficient growth ($M = 10$) as would occur during a surface transition.

Additional scenarios are simulated using different particle sizes, aspect ratios, transition lengths (r_0 to r_f in Equation 3.1), growth modes, and critical supersaturations. The results are much the same as shown by Figure 3.8a with only the simulations with a variable M residing entirely in the $P < 1/3$ region. It is important to note that the classical faceted growth model (constant M) can produce $P < 1/3$ at the beginning of particle growth, with P increasing to values greater than 1/3 (Figure 3.8b). For the simulation to cross the $P = 1/3$ line, the modeled particle must be columnar (planar particles will not produce this result) and the critical supersaturation must be approximately equal to the ambient supersaturation. It is possible that this occurred during the growth of particles #6 and 8. Notice that the P_{ave} values of these two particles are less than 1/3, but Figure 3.7 shows that $P > 1/3$ at the end of their growth cycles. Since simulations with variable M values do not have P ever exceeding 1/3, it is plausible that particles #6 and 8 were non-isometric crystals and growing by 2D ledge nucleation.

Since the behavior of P for half of the grown particles (#2, 3, 4, 5, and 9) can only be modeled by the inclusion of a variable M surface transition, further impacts of the transition are explored theoretically with the KLAH model. The impact a surface transition may have on the effective diffusivity is shown in Figure 3.8c. Again, the simulations with classical, faceted growth theory (constant M) behave as expected; the normalized diffusivity (D/D_0) increases with size, and does so fastest at lower supersaturations. Since the effective diffusivity is normalized by its initial value, only the degree of kinetics limitation can be determined by the power law that describes the variation of D with particle size (Equation 2.9). Recall that in Equation 2.9, the exponent on the effective diffusivity's radius dependence is $1 - n$, where $n = 0$ at the kinetics limit, and $n = 1$ at the diffusion limit. Hence, D is proportional to the particle radius with kinetics-limited growth, whereas it is constant for diffusion-limited growth. Unlike the classical, faceted growth theory

results, the simulations with a variable M (surface transition) have *deceasing* normalized diffusivities, with the decrease occurring most rapidly at low supersaturation.

Since the normalized diffusivity decreases with size when M increases from 1 to 10 (i.e., efficient growth to inefficient growth transition), constant mass growth rates (such as that of particle #5) can be produced, and this is the only way they can be produced. Moreover, half of the data have P values that never exceed 1/3, indicating that the model requires a variable M to explain them. Thus, these data analyses and theoretical simulations support the hypothesis that growth mode changes, or surface transitions, maybe occurring on the homogeneously frozen particles.

3.5 Scale Analysis Results

Further evidence of ice crystal surface transitions appears when the scale analysis method detailed in Section 2.7 is applied to the data. With this analysis method, it becomes easy to distinguish among ice particles that follow classical diffusion-kinetics limited growth with a constant M for faceted ice, those that follow diffusion-limited growth, and those that indicate that they may have experienced a surface transition. Such a distinction can be seen in Figure 3.9, which shows example theoretical calculations with the KLAH model. When the mass ratio m_r is plotted against the logarithm of the scaled mass growth rate ratio $\ln \dot{m}_s$ (Figure 3.9), the diffusion and kinetic limits intersect once. Particle growth modeled with the classical, faceted growth theory (constant M) remains between the diffusion and kinetics limits, and the resulting curves pivot about the point of intersection. Figure 3.9 demonstrates that increasing α by two orders of magnitude simply tilts the modeled growth from the kinetics limit to the diffusion limit. Notice that the curves

become easier to distinguish with lower deposition coefficients, especially for values less than 0.05, which is consistent with the conclusion of Section 2.5.

Particles #8 and 10 serve as clear examples of this technique's utility, with the classic result for a faceted crystal appearing in both the data and in the cubic fit (Figure 3.10, Figure 3.11). In the case of each particle, the data points fall between the diffusion and kinetic limits. Furthermore, modeled growth curves with $M = 10$ fit the data exceptionally well. The model curves highlight that particle #8 has nearly diffusion-limited growth with an average deposition coefficient near 0.05. This particle's results support the discussion in Section 2.5 since the data indicate the presence of diffusion-kinetics limited growth, but no certain statement can be made about the influence of surface attachment kinetics in this case. On the other hand, #10 is clearly closer to the kinetic limit with an average deposition coefficient of 0.006. Particles #1, 6, and 7 likewise have growth bounded by the diffusion and kinetic limits (Table 3.6). In these cases, it is possible to predict the deposition coefficient and critical supersaturation with less uncertainty than in the direct fits to the mass timeseries, which rely on estimated ice supersaturation values. Additionally, by using Equation 2.32, I can estimate a plausible range ice supersaturation for these cases.

To approximate the uncertainty on the determined deposition coefficient, I repeated the scale analysis on the data after first applying a low-pass filter to remove the low frequency oscillations from the data that differentiation amplifies (Figure 3.10b, Figure 3.1b). The α values calculated from the filtered data alone are uncertain due to the low frequency oscillation in the data. However, these values are within the range of the α values derived from the cubic fits for particles #1, 6, 7, and 10 (Table 3.6). Essentially, the same conclusions are drawn from the data when using model fits to the filtered data and when using model fits to the cubic splines. The uncertainty range on the deposition coefficient for particle #8 is very large since its growth is near

the diffusion limit where the resolution on α is poor (see Section 2.5). Consequently, it is not possible to determine a robust deposition coefficient for particle #8. Regardless, the exact value of the deposition coefficient of particles like #8 is of little importance, as, in this case, the surface attachment kinetics only have small impact on the overall mass growth.

The remaining ice particles (#2, 3, 4, 5, and 9) all show signs of surface transitions. Graphically, the surface transitions manifest themselves as curves that begin with a scaled mass growth rate that exceeds that of the constant-M diffusion limit, but the curve falls below that limit as the particle grows (Figure 3.12). When modeling the growth of these particles with the classical model and $M = 10$, the diffusion limit curve is the best fit, which produces a large deposition coefficient. This is a result of the classical model being restricted to the diffusion and kinetic limits, as shown in Figure 3.9. However, if the growth is simulated using a transition from efficient to inefficient growth (variable M in Equation 3.1), then a fit to the data is possible (Figure 3.12 for particle #5). Note that both the data and the model fit reside outside of the diffusion and kinetic limits for classical, faceted ice crystal growth. Since the variation of M rapidly decreases the deposition coefficient, one cannot derive a single α value in these cases (Figure 3.13). When ice particles are small (like the ones in the levitation diffusion chamber), the deposition coefficient changes little with size when using the classical, faceted growth model. Thus, the average value of the deposition coefficient suffices in describing faceted growth.

Table 3.6 details the results of the scale analysis for each ice particle's growth. Comparing these results to those of Table 3.4, the utility of this new analysis method becomes apparent. Half of the particles are best fit with a surface transition model (variable M), thus using a single value of α is not justifiable. Additionally, the critical supersaturations determined better reflect past results (e.g. Libbrecht, 2003; Libbrecht and Rickerby, 2013). Furthermore, recall that the KLAH

model could not fit the timeseries of particle #6 and 10 well enough to determine any meaningful

α or S_{crit}: The model produced high values of α (near unity) and extremely low values of S_{crit}.

However, the scale analysis reveals that particle #6 and 10 likely had classical, faceted growth. In

fact, this new scale analysis method generates deposition coefficients (non-transitioning only) and

critical supersaturations that are reasonable for all of the particle growth data. Moreover, this

method unveils the extent to which the uncertainty on the ice supersaturation affects the

conclusions drawn from the growth data. The diffusion chamber model generally produced a

supersaturation uncertainty of $\sim \pm 1\%$, but this may be a low estimate with the uncertainty actually

being much higher. For instance, if the supersaturation error range is instead taken to be between

the chamber model's mean and the supersaturation derived from Equation 2.32, it becomes clear

that the uncertainty is likely larger than the original estimates. While the uncertainty range may

be less than 4% in some cases (particles #2, 3, 6, and 7), it can reach up to 10% (particle #5).

Table 3.6 Scale analysis results

The following are the results of the scale analysis. The range on the deposition coefficients is determined by analyzing both the smoothed data and the data's cubic fit. Some particles are best fit using a variable M and are indicated by an arrow pointing from the initial to final deposition coefficients (from the cubic fit). The uncertainty on the ice supersaturation originates from the value derived by this analysis and the value produced by the diffusion chamber model. The critical supersaturation values are determined by initiating the diffusion-kinetic model with the ice supersaturation extrema.

Particle #	α	S_{crit} (%)	S_i (%)
20160614-132805 (1)	0.018 – 0.066	6.5 – 12.8	7.8 – 15.4
20160614-143412 (2)	0.078 → 0.021	5.8 – 6.6	13.6 – 15.4
20160614-154240 (3)	0.080 → 0.025	5.8 – 7.3	12.3 – 15.4
20160628-144717 (4)	0.092 → 0.021	2.2 – 4.4	5.4 – 11.0
20160628-152650 (5)	0.034 → 0.002	1.1 – 11.1	1.1 – 11.0
20160726-112828 (6)	0.008 – 0.02	17.9 – 23.2	12.1 – 15.7
20160726-124528 (7)	0.001*	25.7 – 31.7	12.7 – 15.7
20160801-142906 (8)	0.048 – 0.5	14.7 – 17.4	14.9 – 17.3
20160809-130942 (9)	0.126 → 0.042	3.0 – 5.1	14.6 – 25.5
20160809-135510 (10)	0.006 – 0.014	23.4 – 36.0	14.6 – 22.4

*Both analyses have $\alpha = 0.001$ set as a lower limit, and both determined particle #7 to be at or below that limit.

3.6 The Current Work and Past Data

The scale analysis method is especially promising when comparing the results in Table 3.6 and Figure 3.11 through 3.13 to past data. Magee et al. (2006) found the deposition coefficient to be about 0.006 at -40 °C and 0.009 at -44 °C. About 40% of the particles studied this work have deposition coefficients, as determined by the scale analysis method, that resemble values of Magee et al. (2006). Moreover, the critical supersaturation values determined from the Magee et al. (2006) data and this work follow a trend of S_{crit} increasing as the temperature decreases (Figure 1.7, Harrington et al., 2018).

The scale analysis and power law analysis have also been used by our group to re-analyze the data from Harrison et al. (2016) (Harrington et al., 2018). Note that the classical, faceted growth model could typically fit the mass ratio timeseries as was clearly demonstrated in Harrison et al. (2016). Regardless, the scale analysis method cleanly fits the data as is shown in Figure 3.14 (Harrington et al., 2018). Also, it provides more robust deposition coefficient estimates for particles grown in low ice supersaturations. Originally, the deposition coefficients estimated in Harrison et al. (2016) never exceeded 0.05, but those estimates were determined from model fits to the mass timeseries data, which were influenced by uncertainty in the ice supersaturation. However, as Figure 3.14a clearly indicates, the particle that Harrison et al. (2016) grew at -33 °C likely experienced growth limited primarily by diffusion. It is evident that this analysis supports the utility of the scaling methods for determining the deposition coefficient.

Furthermore, the power law analysis results of the Harrison et al. (2016) data reveals a distinct pattern, especially when compared to the data from this work as a function of α (Figure 3.15, Harrington et al., 2018). The re-analysis results from Harrison et al. (2016) show a strong

correlation between the deposition coefficient and the effective diffusivity power law. This is in contrast to the relationship between the deposition coefficient and temperature, shown in Figure 1.3, which is very scattered. However, as Figure 3.15 demonstrates, applying an appropriate scaling analysis to the data produces organization. Moreover, the dashed line in Figure 3.15 shows the relationship between P and α as predicted by a ledge growth model. The data from Harrison et al. (2016) closely fit the ledge growth model curve, suggesting the that heterogeneously nucleated ice particles in that study grew by a surface ledge mechanism. In contrast, every particle with a surface transition, marked with a range on the deposition coefficient, has a power law that falls below the diffusion-limited growth line. Only one non-transitioning particle resides explicitly in the $P < 1/3$ region, and I hypothesized that this occurs because the particle was columnar. Third, the few particles in the $1/3 < P < 2/3$ range appear to all follow the classical ledge nucleation model.

When compared to past results and data, the two analysis methods produced by this work garner support. The results of Magee et al. (2006) suggest that the values of the deposition coefficient and critical supersaturations for my data determined by the scale analysis are reasonable. Moreover, using the scale analysis on the data of Harrison et al. (2016) produced reliable model fits. Furthermore, the power law analysis of the Harrison et al. (2016) data suggests that there may be an underlying relationship between α and P that warrants further investigation. This relationship appears to be robust, which may allow it to serve as a basis for model parameterizations.

Chapter 4

Summary and Conclusion

The growth of ice crystals from water vapor in cold atmosphere clouds is poorly understood and oversimplified in all cloud models. Most cloud models ignore the effects of surface attachment kinetics entirely, opting to instead assume that all ice crystals experience diffusion-limited growth. When cloud models do approximate attachment kinetics, they assume a constant deposition coefficient for all particles, regardless of the particle size, shape, or length of growth time. The sparse experimental results of ice particle deposition coefficients reveal that the surface attachment kinetics often dictates particle growth, more so than vapor diffusion alone. The deposition coefficient, the numerical representation of the growth efficiency of ice, is thus known to often be $\alpha \ll 1$, even though cloud models assume it to be unity. As a result, cloud models likely overpredict growth in low saturation environments and have the wrong growth size dependence (Harrison et al., 2016).

This work builds upon past laboratory studies of the deposition coefficient by investigating ice particle vapor growth at temperatures between -43.4 and -40.2 °C. The ice particles were formed from homogeneously frozen droplets, as can occur in high cirrus clouds. The particles, ranging from about 8 to 22 microns in initial radius, grew in a levitation diffusion chamber with ambient ice supersaturations of 1.1 to 25.5%.

The data were first analyzed fitting the measured mass ratio timeseries with diffusion-kinetics model simulations. The intent was to use the best fit to estimate the particle deposition

coefficient.   However, this analysis produced values of α with significant uncertainty.   One problem of directly analyzing the timeseries is that it depends on the ambient supersaturation, which is constant, but contains substantial uncertainty. Further analysis found that uncertainties that cause as small as a 5% error in the particle mass result in large errors when determining values of α above about 0.05. For example, if a particle actually grew with an $\alpha = 0.1$, the model would not be able to distinguish this value as opposed to a deposition coefficient between 0.023 and 1.

To avoid the uncertainty caused by the supersaturation dependence, two new analysis methods were developed. The first was a power law on the ice particle growth and effective diffusivity. It was demonstrated that a power law function dependent on the ice crystal radius approximates the effective diffusivity well. Furthermore, the exponent of the power law gives a qualitative understanding of an ice particle's deposition coefficient where $P = 1/3$ applies to diffusion-limited growth, while $P = 2/3$ applies to kinetics-limited growth. Interestingly, the average values of P for my experiments were 0.146 – 0.643, with more than half of the particles producing $P_{ave} < 1/3$. The diffusion-kinetics model was only able to replicate the $P_{ave} < 1/3$ behavior with the introduction of a model of a surface transition.

Physically, a surface transition represents the ice particle's transformation from efficient growth, with many ledges to serve as vapor attachment sites, to inefficient growth, with few attachment sites on the ice surface. Surface transitions are known to occur while particles evolve, especially as crystals form from frozen droplets.   Even so, we lack a growth model this phenomenon. A surface transition can be modeled, in approximation, by increasing the ice growth mechanism parameter, M, which represents mechanism by which attachment sites form on the ice surface. Consequently, increasing M rapidly decreases the deposition coefficient, which in turn decreases the effective diffusivity.

Further evidence of surface transitions occurring on some of the particles grown in the diffusion chamber appears by using a second new analysis technique. The deposition coefficient and chamber ice supersaturation can also be estimated with this technique. The growth data were scaled by the mean growth rate ratio to remove the dependence on the supersaturation. Using this analysis, the diffusion-kinetics model fit half of the ice particles with α values of $0.001 - 0.5$. The other half could only be fit when an approximate model surface transitions was used. The scale analysis was able to determine deposition coefficients for some particles whose timeseries could not be fit easily with the classical, faceted growth model (constant M). Scale analysis also gave a clear signal when a particle likely experienced a surface transition.

A transitioning ice crystal surface is not new, but it has never been considered in studies of the deposition coefficient. The inconsistencies between laboratory results of deposition coefficients may be explained, in part, by the occurrence of surface transitions on the ice particles. Many of prior studies begin recording ice crystal growth measurements promptly following nucleation (e.g. Magee et al., 2006; Earle et al., 2010; Skrotzki et al., 2013), a period in which surface transitions likely occur. In the future, work should focus on imaging the ice surface as transitions occur. Additionally, the model's approximation of a surface transition that I developed in this thesis should be tested and improved. Further, the new analysis techniques should be tested on more datasets of particles in a wider range of conditions. Perhaps if the impacts of ice crystal surface transitions are thoroughly quantified, the accuracy of cloud models can be improved.

Appendix

List of Variables

Variable	Definition
α	Deposition coefficient
S_{local}	Supersaturation at ice surface
S_{crit}	Critical supersaturation for nucleation
M	Growth mechanism
$\frac{dm}{dt}, \dot{m}$	Particle mass growth rate
C	Particle shape capacitance
D	Effective diffusivity
S_i	Ambient ice supersaturation
T_∞	Ambient temperature
p	Pressure
c	Prism axis semi-length
a	Basal axis semi-length
α_c	Prism facet deposition coefficient
α_a	Basal facet deposition coefficient
D_v'	Modified vapor diffusivity
k_T'	Modified thermal diffusivity
R	Universal gas constant

M_w	Molar mass of water
e_i	Equilibrium vapor pressure over ice
l_s	Enthalpy of sublimation
D_v	Vapor diffusivity
$\overline{v_v}$	Mean vapor molecule speed
C_Δ	Particle capacitance with vapor jump
k_T	Thermal diffusivity
$\alpha_{T,a}$	Basal thermal accommodation coefficient
$\alpha_{T,c}$	Prism thermal accommodation coefficient
ρ_a	Air density
c_p	Specific heat of air at constant pressure
$\overline{v_a}$	Mean air molecule speed
ε	Mass error
m_t	True particle mass
m_i	Incorrect particle mass
α_t	Ture deposition coefficient
α_i	Predicted deposition coefficient
$\dot{m}_0$	Initial particle mass growth rate
r	Equivalent-volume sphere radius
r_0	Initial equivalent-volume sphere radius
D_0	Initial effective diffusivity

α_0	Initial deposition coefficient
n	Power on deposition coefficient
m	Particle mass
m_0	Initial particle mass
P	Particle mass growth power law
D	Diffusivity of vapor and heat
ρ_i	Density of ice
$\dot{m}_r$	Mass growth rate ratio
m_r	Mass ratio
κ	Mass growth rate ratio constant
$\overline{v_v}$	Mean molecular vapor speed
ρ_{eq}	Equilibrium vapor density
$\dot{m}_s$	Scaled mass growth rate ratio
$\overline{D_r}$	Radius-weighted average diffusivity
P_{ave}	Average growth power law exponent
r_f	Final particle radius

BIBLIOGRAPHY

Bacon, N. J., M. B. Baker, and B. D. Swanson, 2003: Initial stages in the morphological evolution of vapour-grown ice crystals: A laboratory investigation. *Q.J.R.Meteorol.Soc.,* **129**, 1903-1927, doi:10.1256/qj.02.04.

Brown, D., S., George, C. Huang, E. Wong, K. Rider, R. Smith, and B. Kay, 1996: H2O condensation coefficient and the refractive index for vapor-deposited ice from molecular beam and optical interference measurements. *J. Phys. Chem.*, **100**, 4988-4995, doi: 10.1021/jp952547j.

Bailey, M. P., J. Hallett, 2009: A Comprehensive Habit Diagram for Atmospheric Ice Crystals: Confirmation from the Laboratory, AIRS II, and Other Field Studies. *J.Atmos.Sci.,* **66**, 2888-2899, doi:10.1175/2009JAS2883.1.

Burton, W. K., N. Cabrera, and F. C. Frank, 1951: The Growth of Crystals and the Equilibrium Structure of their Surfaces. *Philosophical Transactions of the Royal Society of London.Series A, Mathematical and Physical Sciences,* **243**, 299-358, doi:10.1098/rsta.1951.0006.

Chen, J., D. Lamb, 1994: The Theoretical Basis for the Parameterization of Ice Crystal Habits: Growth by Vapor Deposition. *J.Atmos.Sci.,* **51**, 1206-1222, doi:10.1175/1520-0469(1994)051

Choularton, T., and J. Latham, 1977: Measurements of the deposition coefficient for ice, and its application to cirrus seeding. *Quart. J. Roy. Meteor. Soc.*, **103**, 307–318, doi:10.1002/qj.49710343608.

Earle, M., T. Kuhn, A. Khalizov, and J. Sloan, 2010: Volume nucleation rates for homogeneous freezing in supercooled water microdroplets: Results from a combined experimental and modeling approach. *Atmos. Chem. Phys*., **10**, 7945–7961, doi:10.5194/acp-10-7945-2010.

Elbaum, M., 1991: Roughening transition observed on the prism facet of ice. *Phys. Rev. Lett*., **67** (21), 2982−2985.

Elliott, W. J., 1971: Dimensions of thermal diffusion chambers. J.Atmos. Sci., 28, 810–811, doi:10.1175/1520-0469(1971)028,0810: DOTDC.2.0.CO;2.

Gierens, K. M., M. Monier, and J. Gayet, 2003: The deposition coefficient and its role for cirrus clouds. *Journal of Geophysical Research: Atmospheres,* **108**, - 4069, doi:10.1029/2001JD001558.

Gonda, T. and T. Yamazaki, 1983: Initial Growth forms of Snow Crystals Growing from Frozen Cloud Droplets, *Journal of the Meteorological Society of Japan*, **62**, 190-192, https://doi.org/10.2151/jmsj1965.62.1_190.

Gonda, T., Y. Matsuura, and T. Sei, 1994: In situ observation of vapor-grown ice crystals by laser two-beam interferometry. *Journal of Crystal Growth*. **142**. 171–176. 10.1016/0022-0248(94)90285-2.

Hanson, M., A. Moyle, J. Harrington, 2016: Measurements of vapor growth and sublimation of individually levitated ice particles below -30°C. International Conference on Clouds and Precipitation, Paper 1.14, Manchester, England, July 23-29.

Harrington, J. Y., D. Lamb, and R. Carver, 2009: Parameterization of surface kinetic effects for bulk microphysical models: Influences on simulated cirrus dynamics and structure. *J. Geophys. Res*., **114**, D06212, doi:10.1029/2008JD011050.

Harrington, J.Y., H. Morrison, G. Pokrifka, M. Hanson, and A. Moyle, 2018: On predicting the deposition coefficient in models of ice crystal growth. *J. Atmos. Sci*., in preparation.

Harrington, J. Y., K. Sulia, and H. Morrison, 2013: A Method for Adaptive Habit Prediction in Bulk Microphysical Models. Part I: Theoretical Development. *J.Atmos.Sci.,* **70**, 349-364, doi:10.1175/JAS-D-12-040.1.

Harrington, J. Y., K. Sulia, and H. Morrison, 2013: A Method for Adaptive Habit Prediction in Bulk Microphysical Models. Part II: Parcel Model Corroboration. *J.Atmos.Sci.,* **70**, 365-376, doi:10.1175/JAS-D-12-0152.1.

Harrison, A., 2013: Vapor growth of small ice crystals at low temperatures in an electrodynamic levitation diffusion chamber, M.S. thesis, The Pennsylvania State University.

Harrison, A., A. M. Moyle, M. Hanson, and J. Y. Harrington, 2016: Levitation Diffusion Chamber Measurements of the Mass Growth of Small Ice Crystals from Vapor. *J. Atmos. Sci.,* **73**, 2743–2758, https://doi.org/10.1175/JAS-D-15-0234.1

Haynes, D., N. Tro, and S. George, 1992: Condensation and evaporation of H2O on ice surfaces. *J. Phys. Chem*., **96**, 8502-8509, doi:10.1021/j100200a055.

Kong, X., P. Papagianakopoulos, E.S. Thomson, N. Markovic, and J.B.C. Pettersson, 2014: Water accommodation and desorption kinetics on ice. *J. Phys. Chem*., **118**, 3973−3979.

Korolev, A. V., M.P. Bailey, J. Hallett, and G.A. Isaac, 2004: Laboratory and in situ observation of deposition growth of frozen drops. *J. Appl. Meteor.*, **43,** 612-622.

Lamb, D., and J. Chen, 1995: An expanded parameterization of growth of ice crystals by vapor deposition. Preprints, Conf. on Cloud Physics, Dallas, TX, Amer. Meteor. Soc., 389–392.

Lamb, D., and W.D. Scott, 1974: The Mechanism of Ice Crystal Growth and Habit Formation. *J. Atmos. Sci.*, **31**, 570-580.

Lamb, D., and J. Verlinde, 2011: *The Physics and Chemistry of Clouds*. Cambridge University Press.

Lewis, B., 1974: The growth of crystals of low supersaturation: I. Theory. *J. Cryst. Growth*, **21**, 29–39, doi:10.1016/0022-0248(74)90146-8.

Libbrecht, K., 2003: Growth rates of the principal facets of ice between −10°C and −40°C. *J.Cryst.Growth,* **247**, 530-540, doi:10.1016/S0022-0248(02)01996-6.

Libbrecht, K.G., 2005: The physics of snow crystals. *Rep. on Prog. in Phys.,* **68**, 855. Lamb, D. and W.D. Scott (1972). Linear growth rates of ice crystals grown from the vapor phase. *J. Cryst. Growth*, **12**, 21–31.

Libbrecht, K., and M.E. Rickerby, 2013: Measurements of surface attachment kinetics for faceted ice crystal growth. *J. Cryst. Growth*, **377**,1-8.

Magee, N. B., 2006: A laboratory investigation of vapor-grown ice crystals at low atmospheric temperatures, Ph.D. dissertation, The Pennsylvania State University.

Magee, N., A. Moyle, and D. Lamb, 2006: Experimental determination of the deposition coefficient of small cirrus-like crystals near -50 °C. *Geophys. Res. Lett.*, **33**, L17813, doi:10.1029/2006GL026665.

Nelson, J., 1994: A theoretical study of ice crystal growth in the atmosphere. Ph.D. dissertation, University of Washington, 83 pp.

Nelson, J. T., M. B. Baker, 1996: New theoretical framework for studies of vapor growth and sublimation of small ice crystals in the atmosphere. *J. Geophys. Res.: Atmos.,* **101**, 7033-7047, doi:10.1029/95JD03162.

Nelson, J., C. A. Knight, 1996: A new technique for growing crystals from the vapor. *J.Cryst.Growth,* **169**, 795-797, doi:10.1016/S0022-0248(96)00718-X.

Nelson, J., C. Knight, 1998: Snow Crystal Habit Changes Explained by Layer Nucleation. *J.Atmos.Sci.,* **55**, 1452-1465, doi:10.1175/1520-0469(1998)055

Pedersen C., A. Mihranyan, M. Strømme, 2011: Surface Transition on Ice Induced by the Formation of a Grain Boundary. *PLoS ONE,* **6(9):** e24373. https:/doi.org/10.1371/journal.pone.0024373

Pratte, P., H. van den Bergh, and M. Rossi, 2006: The kinetics of H2O vapor condensation and evaporation on different types of ice in the range of 130–210 K. *J. Phys. Chem*., **110**, 3042-3058, doi:10.1021/jp053974s.

Pruppacher, H. R., J. D. Klett, 1997: *Microphysics of Clouds and Precipitation.* 2nd ed. Vol. 18, Kluwer Academic Publishers.

Sei, T., and T. Gonda, 1989: The growth mechanism and the habit change of ice crystals grown from the vapor phase. *J Crystal Growth*, **94**, 697-707.

Skrotzki, J., P. Connolly, M. Schnaiter, H. Saathoff, O. Möhler, R. Wagner, M. Niemand, V. Ebert, and T. Leisner: The accomodations coefficient of water molecules on ice-cirrus cloud studies at the AIDA simulation chamber, *Atmos. Chem. And Phys*., **13**, 4451-4466, doi:10.5194/acp-13-4451-2013

Swanson, B. D., N. J. Bacon, E. J. Davis, and M. B. Baker, 1999: Electrodynamic trapping and manipulation of ice crystals. *Q.J.R.Meteorol.Soc.,* **125**, 1039-1058, doi:10.1002/qj.49712555514.

Walko, R. L., W. R. Cotton, M. P. Meyers, and J. Y. Harrington, 1995: New RAMS cloud microphysics parameterization part I: the single-moment scheme. *Atmos.Res.,* **38**, 29-62, doi:10.1016/0169-8095(94)00087-T.

Wood, S. E., M. B. Baker, and D. Calhoun, 2001: New model for the vapor growth of hexagonal ice crystals in the atmosphere. *Journal of Geophysical Research: Atmospheres,* **106**, 4845-4870, doi:10.1029/2000JD900338.

Woods, C. P., M. T. Stoelinga, and J. D. Locatelli, 2008: Size Spectra of Snow Particles Measured in Wintertime Precipitation in the Pacific Northwest. *J.Atmos.Sci.,* **65**, 189-205, doi:10.1175/2007JAS2243.1.

Zhang, C., and J. Harrington, 2014: Including surface kinetic effects in simple models of ice vapor diffusion. *J. Atmos. Sci*., **71**, 372–390, doi:10.1175/JAS-D-13-0103.1.

Zhang, C., and J. Y. Harrington, 2015: The effects of surface kinetics on crystal growth and homogeneous freezing in parcel simulations of cirrus. *J. Atmos. Sci*., **72**, 2929–2946, doi:10.1175/JAS-D-14-0285.1.

FIGURES
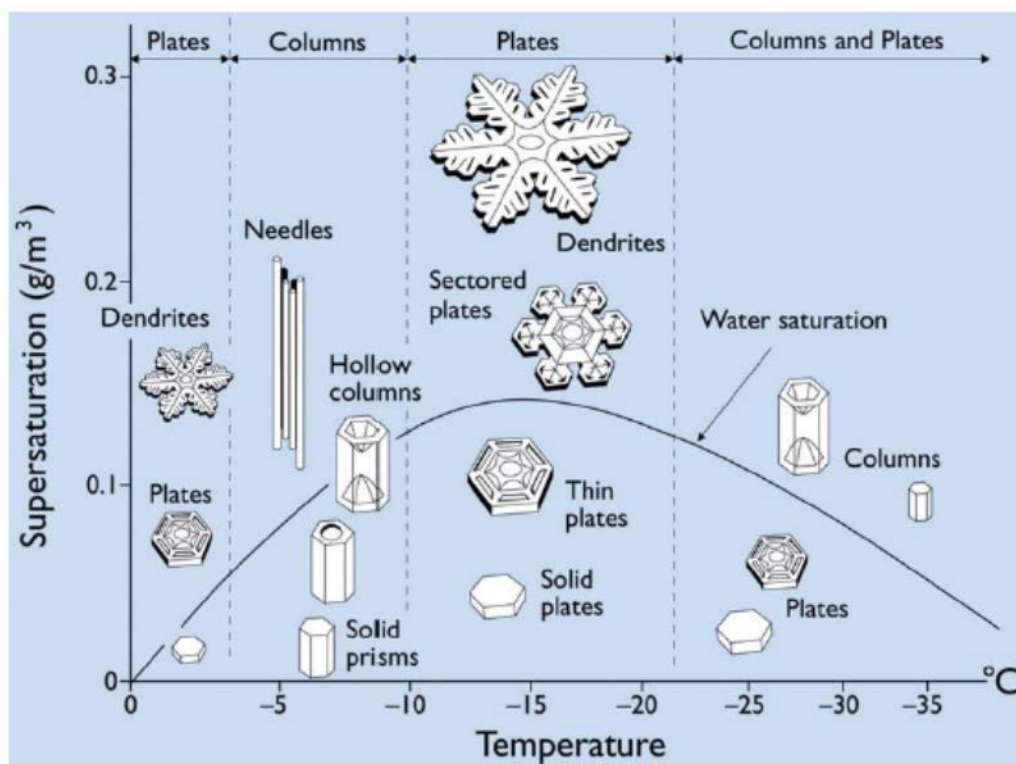
Figure 1.1 Dependence of ice crystal morphology to temperature and saturation

Ice crystal habit depends on temperature, which controls if the crystal is a plate or a column. The habit also gains complexity with higher supersaturation (Libbrecht, 2003).
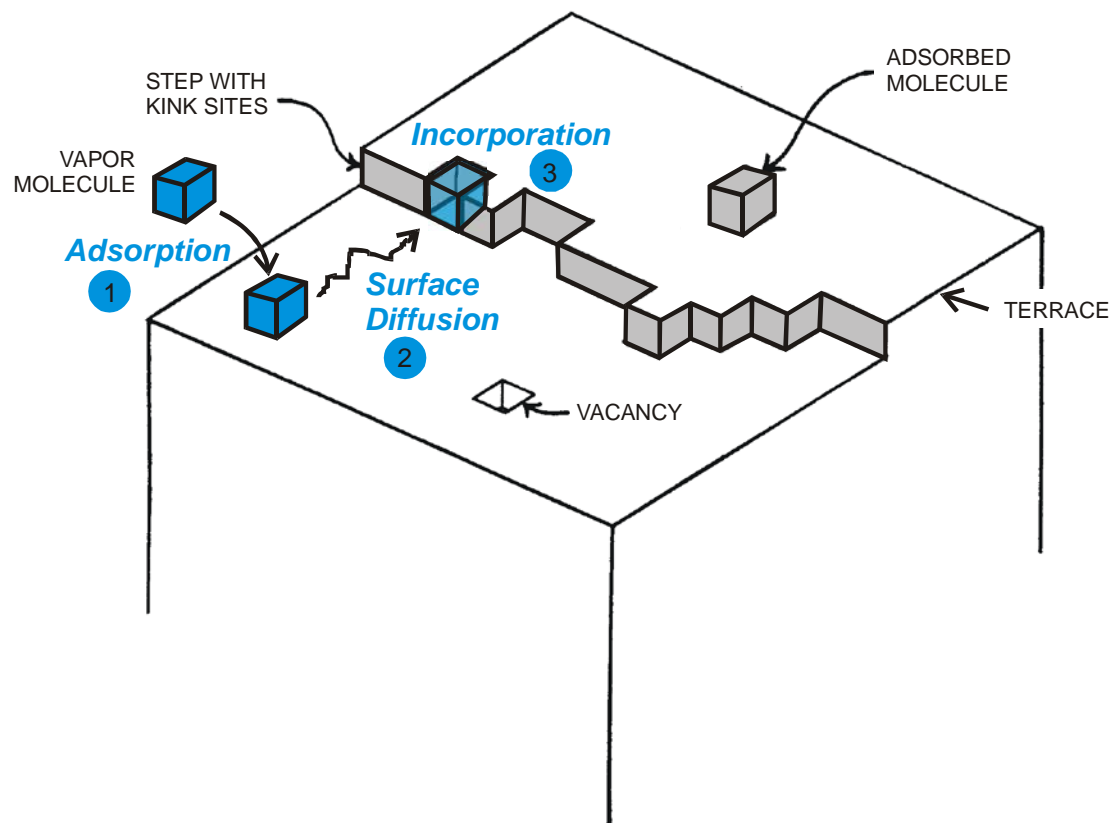
Figure 1.2 Schematic of ice crystal surface attachment kinetics

Vapor molecules that diffuse to the ice particle surface undergo surface attachment kinetics. A kink site is necessary for a molecule to be incorporated, otherwise it will desorb (Lamb and Verlinde, 2011, Figure 8.15).
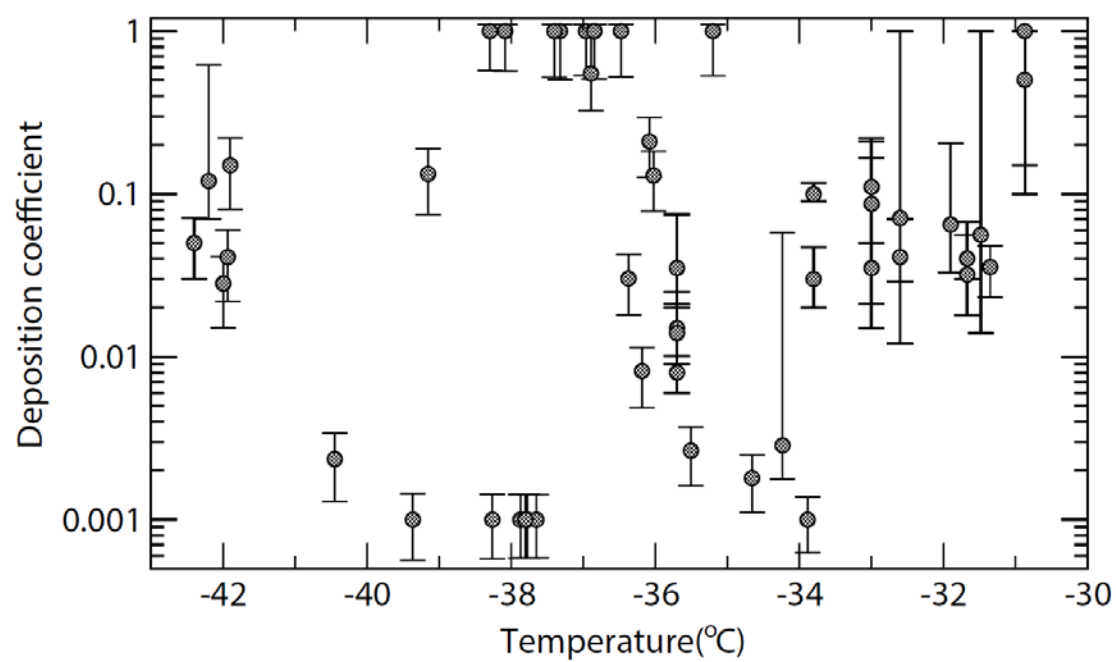
Figure 1.3 Plot of temperature to deposition coefficient

Plotted are all of the deposition coefficient measurements taken from our levitation diffusion chamber. No clear dependence on the temperature emerges. (Harrington et al., 2018)
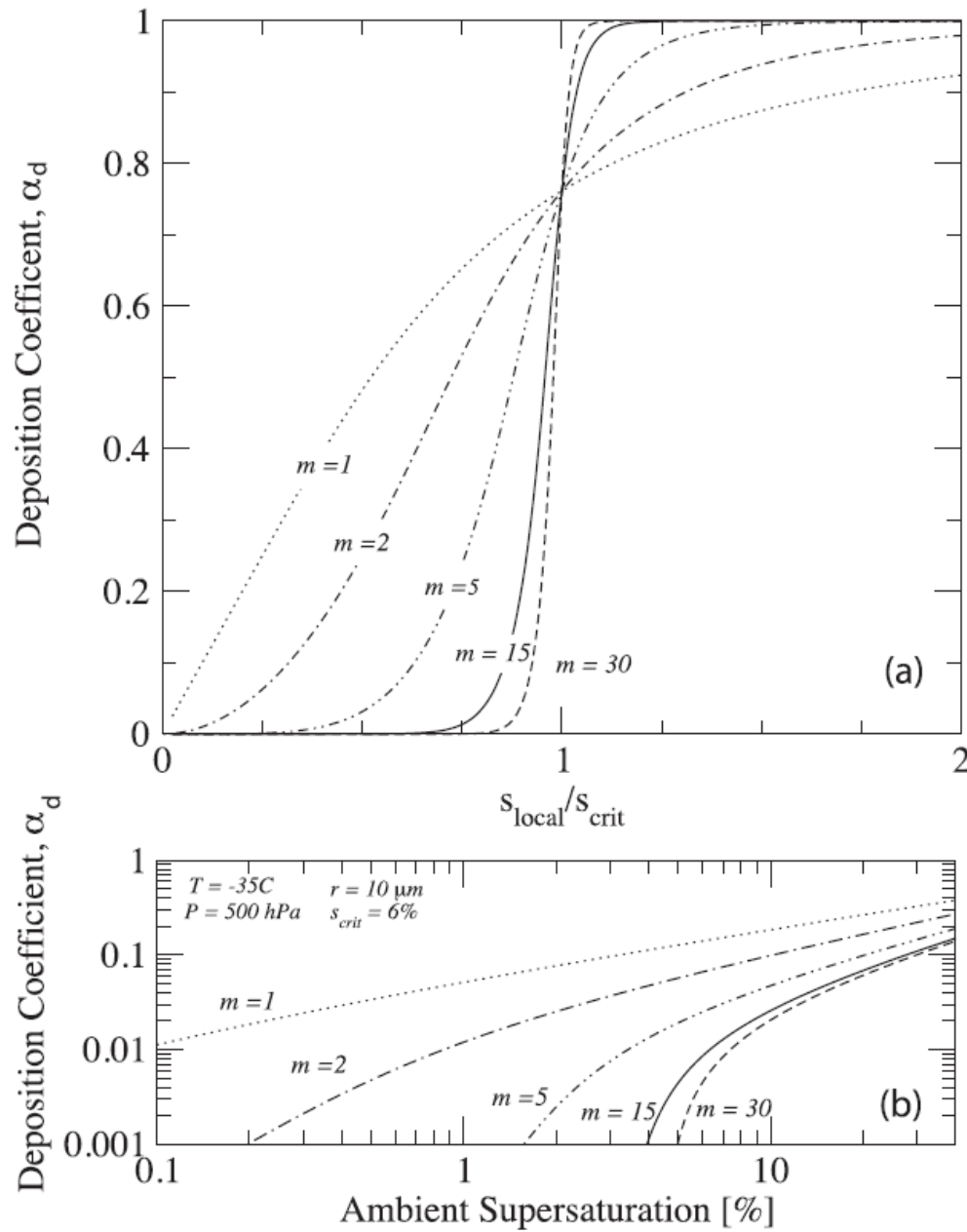
Figure 1.4 Dependence of the deposition coefficient on the growth mechanism

a) The relationship between the ratio of the local supersaturation at the particle surface to the critical supersaturation and the deposition coefficient depends on the growth mechanism parameter (m in this figure). For dislocation growth ($m = 1$), the deposition coefficient is comparatively large regardless of the local supersaturation. For 2-D nucleation ($10 \leq m \leq 30$), the local supersaturation must be near or greater than the critical supersaturation for efficient growth to occur. **b)** The growth mechanism parameter also influences the relation between the ambient supersaturation and the deposition coefficient. Smaller values of m generally increase the deposition coefficient (Zhang and Harrington, 2015, Figure 1).
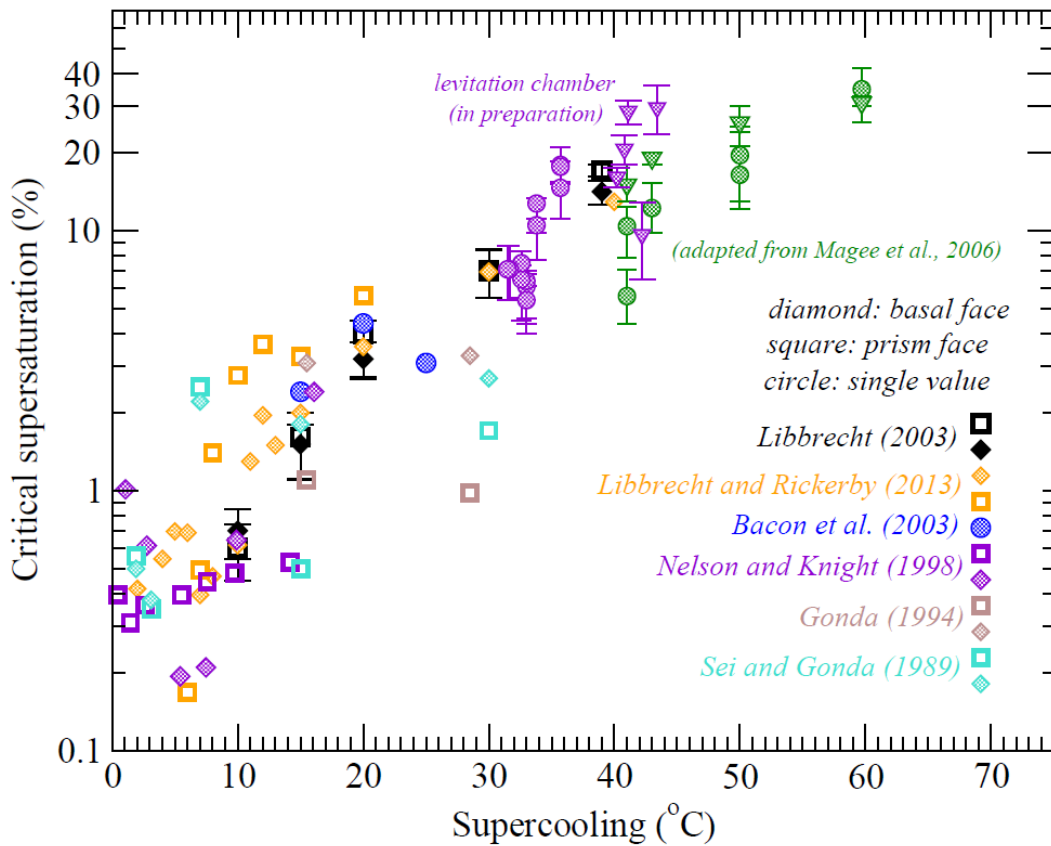
Figure 1.5 Measured critical supersaturation values

Plotted are all of the known measurements of the critical supersaturation. The values taken from the levitation chamber and Magee et al. (2006) were analyzed by our lab group. Note that the purple triangle shown are measurements from the current work. Other than our measurements, there are few critical supersaturation measurements below 20 °C supercooling (Supercooling = 0 °C – T). Laboratory measurements suggest that the Critical supersaturation rises with the supercooling (Harrington at al., 2018).
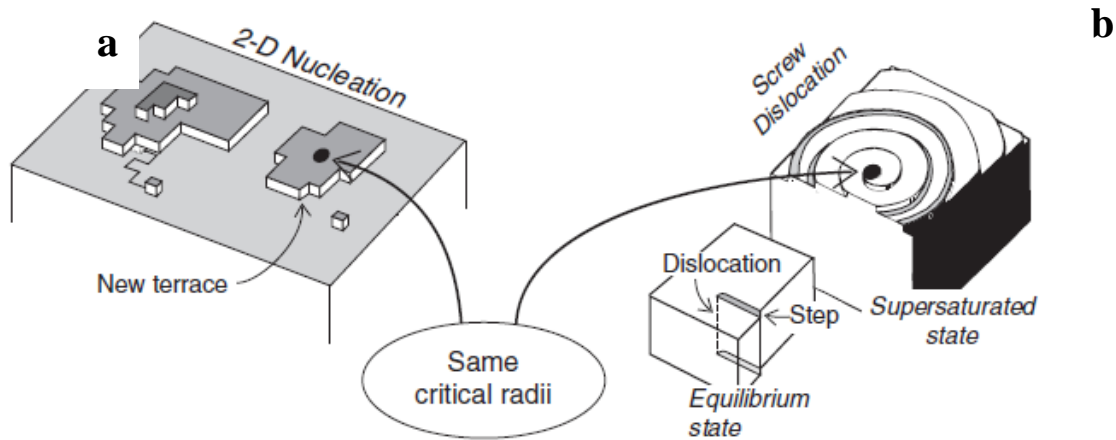
Figure 1.6 Schematic of two growth mechanisms

Diagram of two ice growth modes from vapor. **a)** 2-D Nucleation requires $S_i \geq S_{crit}$ to nucleate ledges to act as attachment points for vapor molecules. **b)** Screw Dislocation utilizes a defect in the ice lattice to continuously form kink sites for new molecules (Lamb and Verlinde, 2011, Figure 8.16).
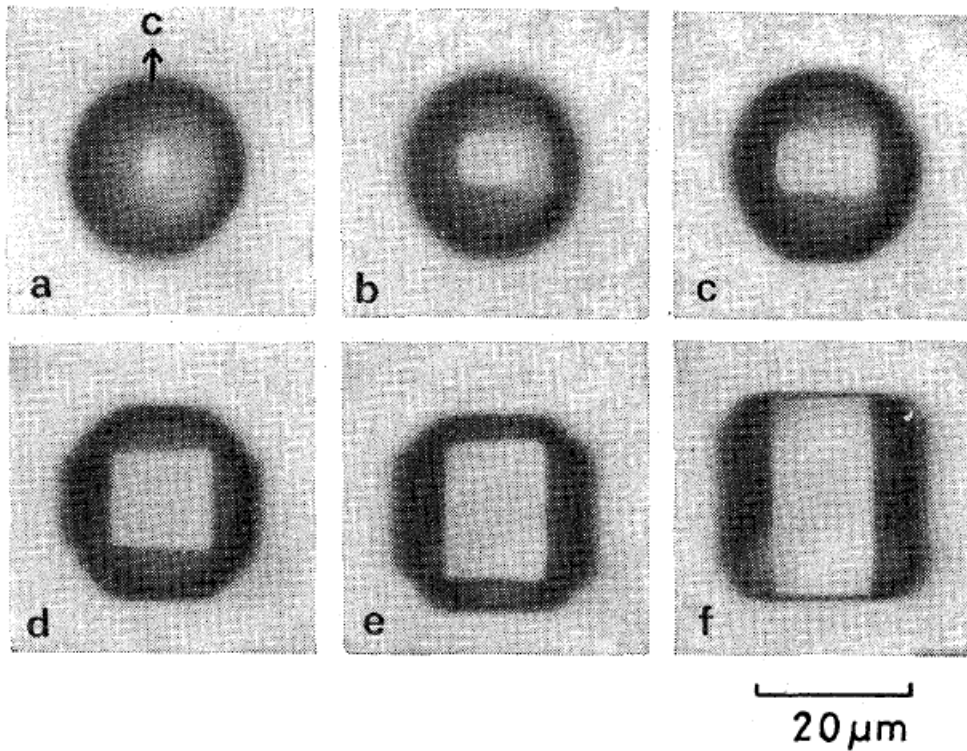
Figure 1.7 Evolution of a frozen droplet to a hexagonal prism

A frozen droplet transitioning to a hexagonal prism. Rapidly growing pyramidal facets are visible in c, d, and e, located between the basal (top/bottom) facets and the prism (side) facets (Gonda and Yamazaki. 1983, Figure 1).

(a) Chamber Side View

drop launcher
(450 V)
and tube

higher temperature
coolant flow

Plexiglas®
housing

copper
plate

plate
thickness
= 2.54 cm

grounded
(Z+)

Plexiglas®
ring

plate
separation
= 1.27 cm

copper
plate

quadrupole
button electrodes
(600 V at 60 Hz)

embedded
thermocouples

Z- voltage
(10 V)

lower temperature
coolant flow

Plexiglas®
housing

(b) Top Plate Interior

Y-axis

outer
diameter
= 17.78 cm

chamber
diameter
= 10.2 cm

Plexiglas®
ring

launch
opening

inner
diameter
= 3.4 cm

X-axis

button
electrodes

circular
windows

viewing
windows

Figure 2.1 Schematic of the levitation diffusion chamber

Schematic of the levitation diffusion chamber used. **a)** The side view of the chamber shows the relative positions of the Plexiglas® cryogen housings, the copper plates, the Plexiglas® chamber wall, and the droplet launcher. **b)** The view of the bottom of the top copper plate reveals the locations of the "dry" regions resulting from the presence of the four button electrodes and the launcher opening (Harrison et al., 2016, Figure 1).
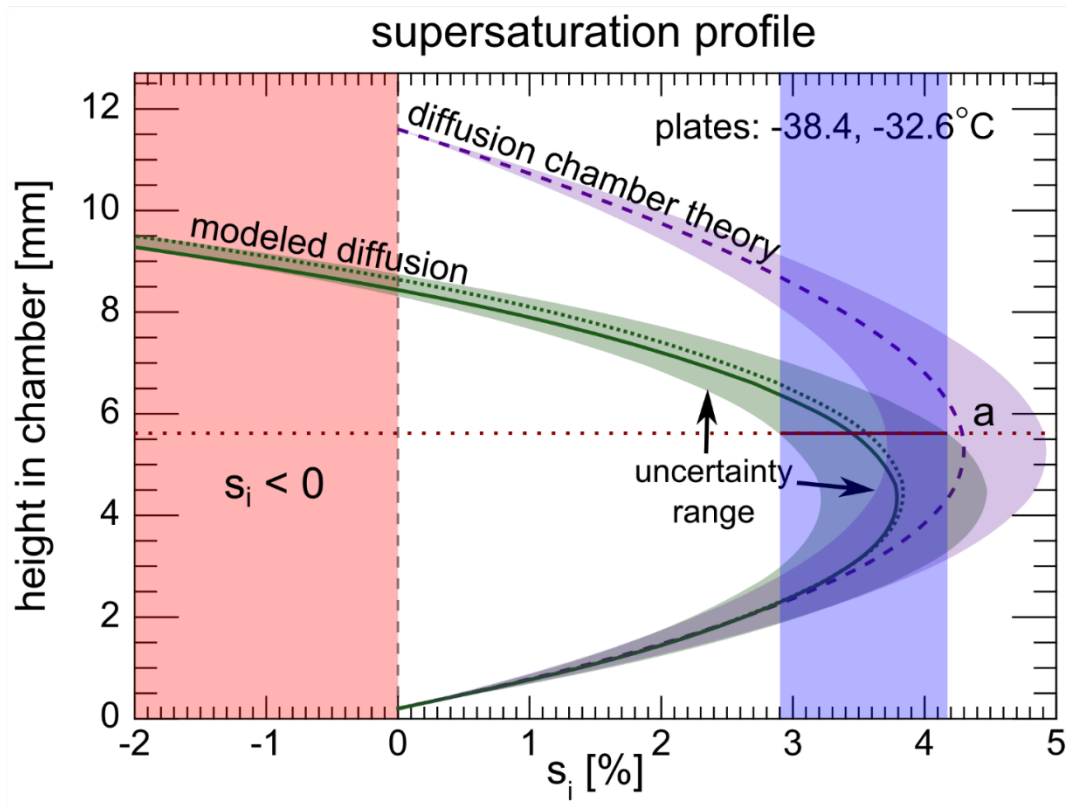
Figure 2.2 Example supersaturation profile from the diffusion chamber model

Ice supersaturation chamber height as given by classic diffusion chamber theory and the diffusion chamber model. In this example, the top copper plate temperature is -32.6 °C, while the bottom plate is at -38.4 °C. Uncertainty ranges arise from uncertainty of the ice thickness on the plates and the moisture content difference due to the electrodes and launcher opening. The blue region indicates the expected supersaturation range for a particle located at 5.6 mm above the chamber floor. In this example, the model predicts S_i to be $2.9 - 4.2\%$, while theory suggests it to be $3.7 - 4.9\%$.
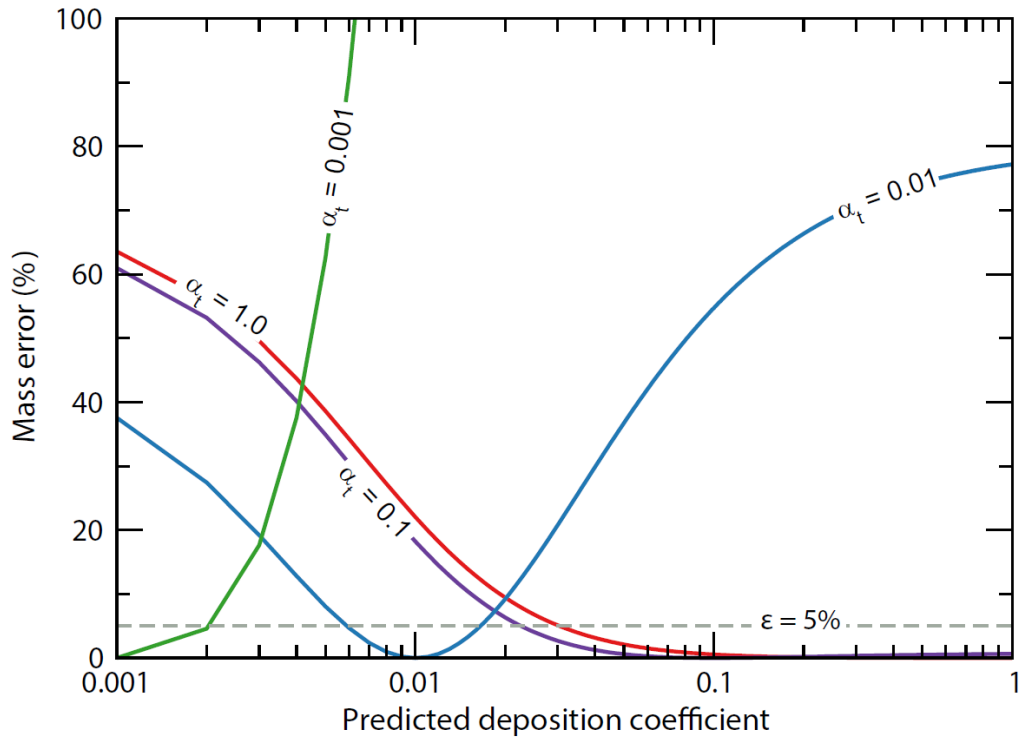
Figure 2.8 Plot of predicated deposition coefficients to mass error

Mass error curves from modeling ice growth based on different deposition coefficients. Each solid curve corresponds to growth with a true deposition coefficient. The mass error is derived from the departure from the true mass when simulating growth using an incorrect deposition coefficient. Additionally, the dashed line marks a 5% mass error. Sections of each solid curve below the dashed line cannot be resolved with a 5% mass error.
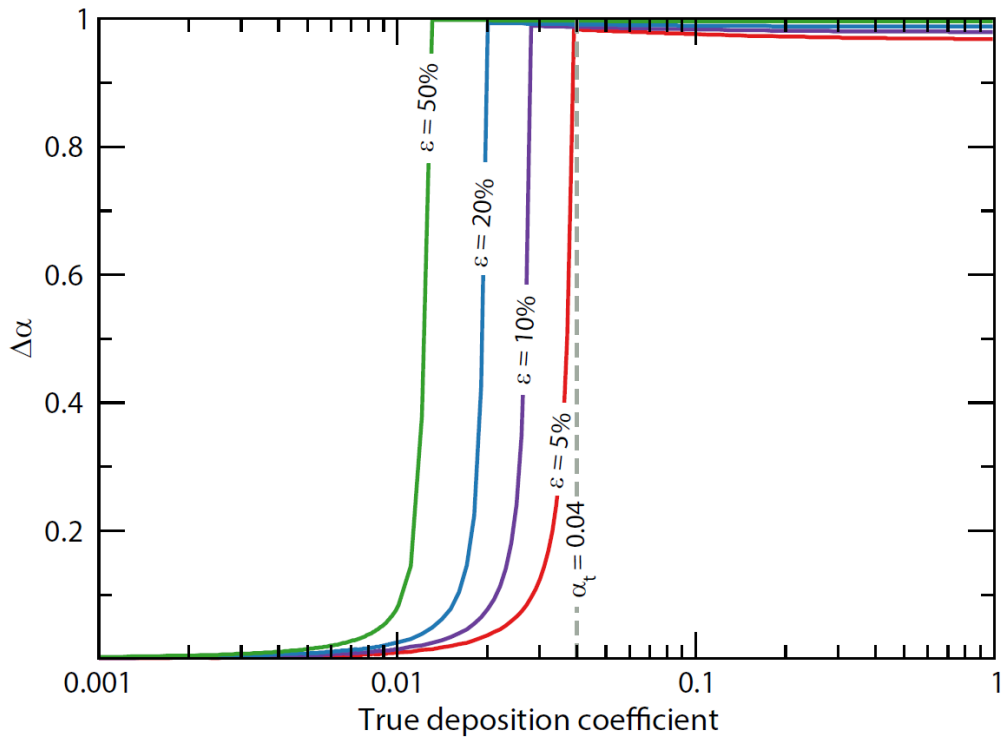
Figure 2.9 Plot of true deposition coefficient perdition resolution

Resolution range of determining the true deposition coefficient for various mass error thresholds. When $\Delta\alpha$ is unity, all resolution is lost. The dashed line is where the true deposition coefficient $\alpha_t = 0.04$. For a mass error 5%, it is nearly impossible to determine the value of the true deposition coefficient when it is greater than or equal to 0.04.
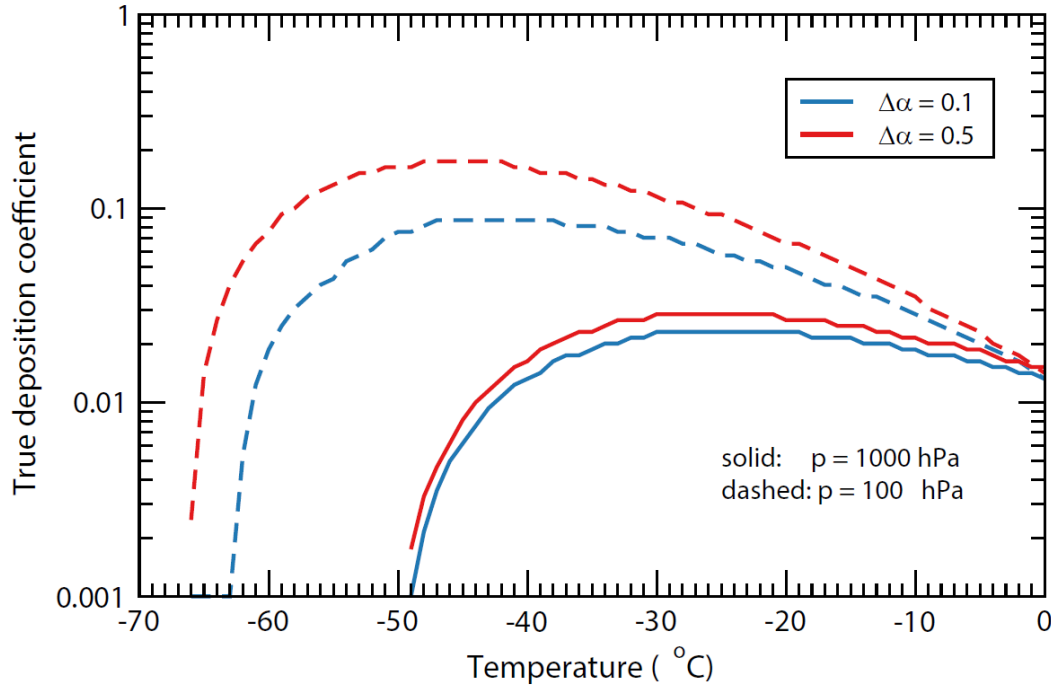
Figure 2.10 Deposition coefficient resolution temperature and pressure dependence

This figure shows the deposition coefficients at which resolution is lost at different temperatures and pressures, with a mass error threshold of 10%. Solid curves are at a pressure of 1000 hPa, and dashed curves are at 100 hPa. The blue curves indicate the deposition coefficient value at which the transition from high to low resolution begins to occur, and the red curves show when the transition is almost complete. Note that more deposition deficient values have a high predication resolution at the lower pressure. Additionally, the resolution rapidly declines for temperatures less than -40 °C at the higher pressure.
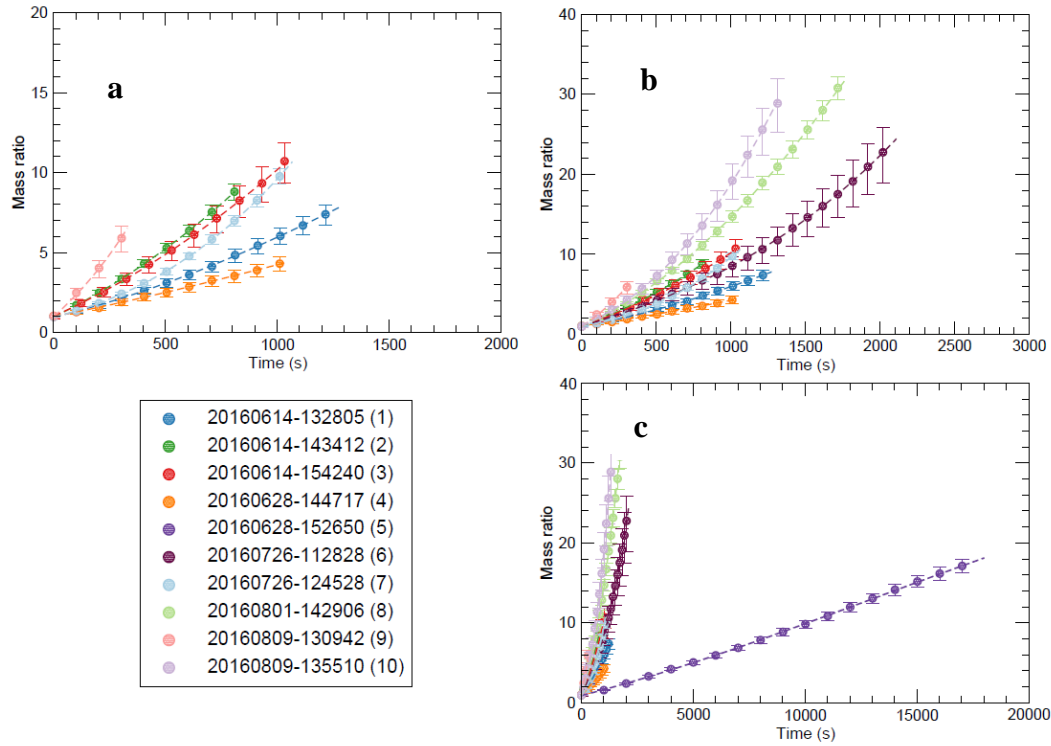
Figure 3.11 Plotted mass ratio timeseries of all ice particles

Mass ratio growth timeseries of ice. Data is shown as points (every hundredth point) with error bars, which originate from uncertainty in the temperature, initial radius, and bottom plate voltage. The dashed lines are cubic fits to the data. Each color represents a separate particle. Each subfigure increases the number of datasets shown with **a)** particles that grew to less than 15 times the original mass, **b)** particles that grew for less than 2500 seconds, and **c)** all particles. Note the changes in axis scales in each subplot.
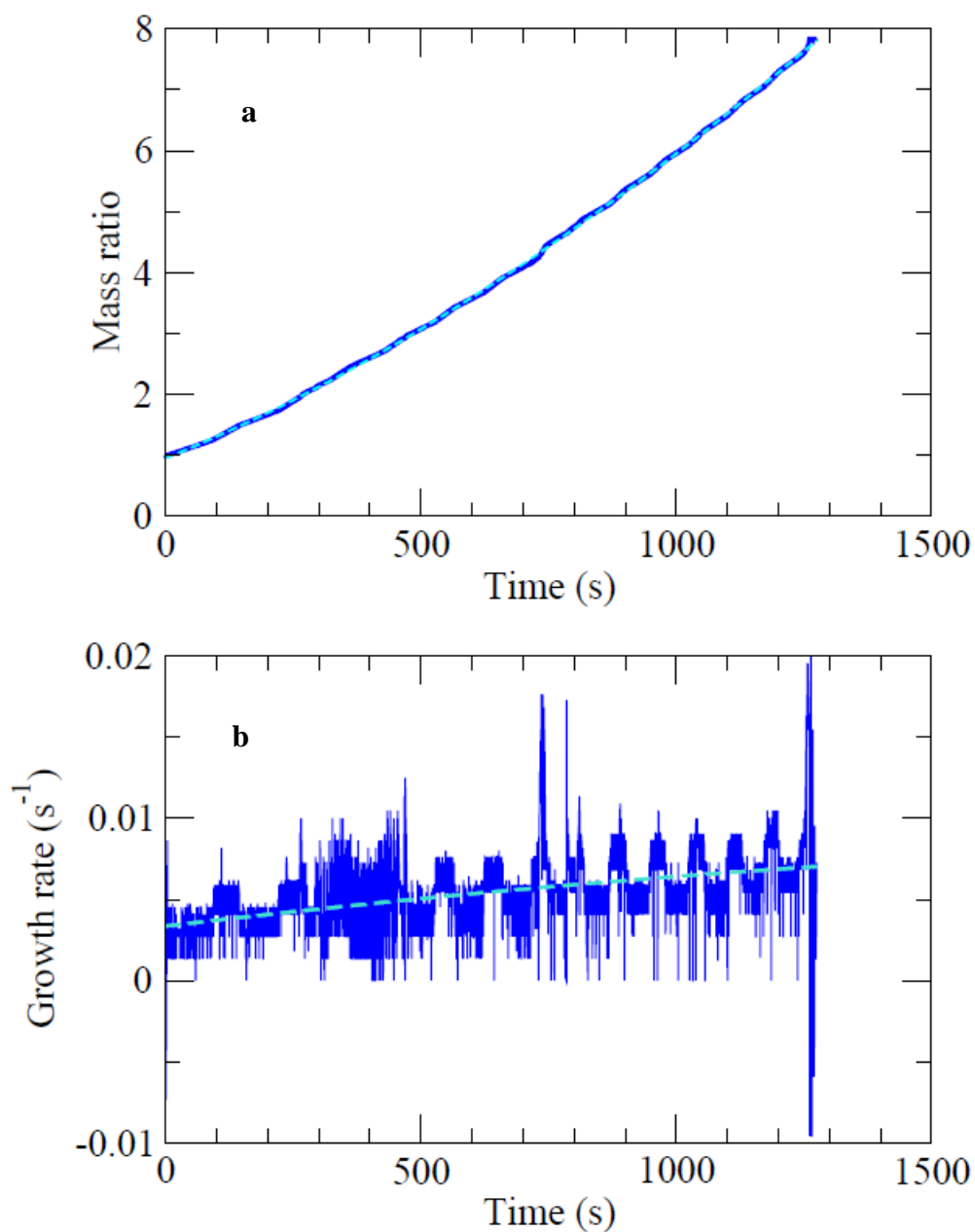
Figure 3.12 The cubic fit and low frequency oscillations in the data

a) Low frequency oscillations appearing in the particle #1 raw mass data. The light dashed curve is the cubic fit to the data. **b)** The oscillations become more obvious in the data's derivative. The derivative of the cubic fit (dashed curve) intersects the middle of the waves.
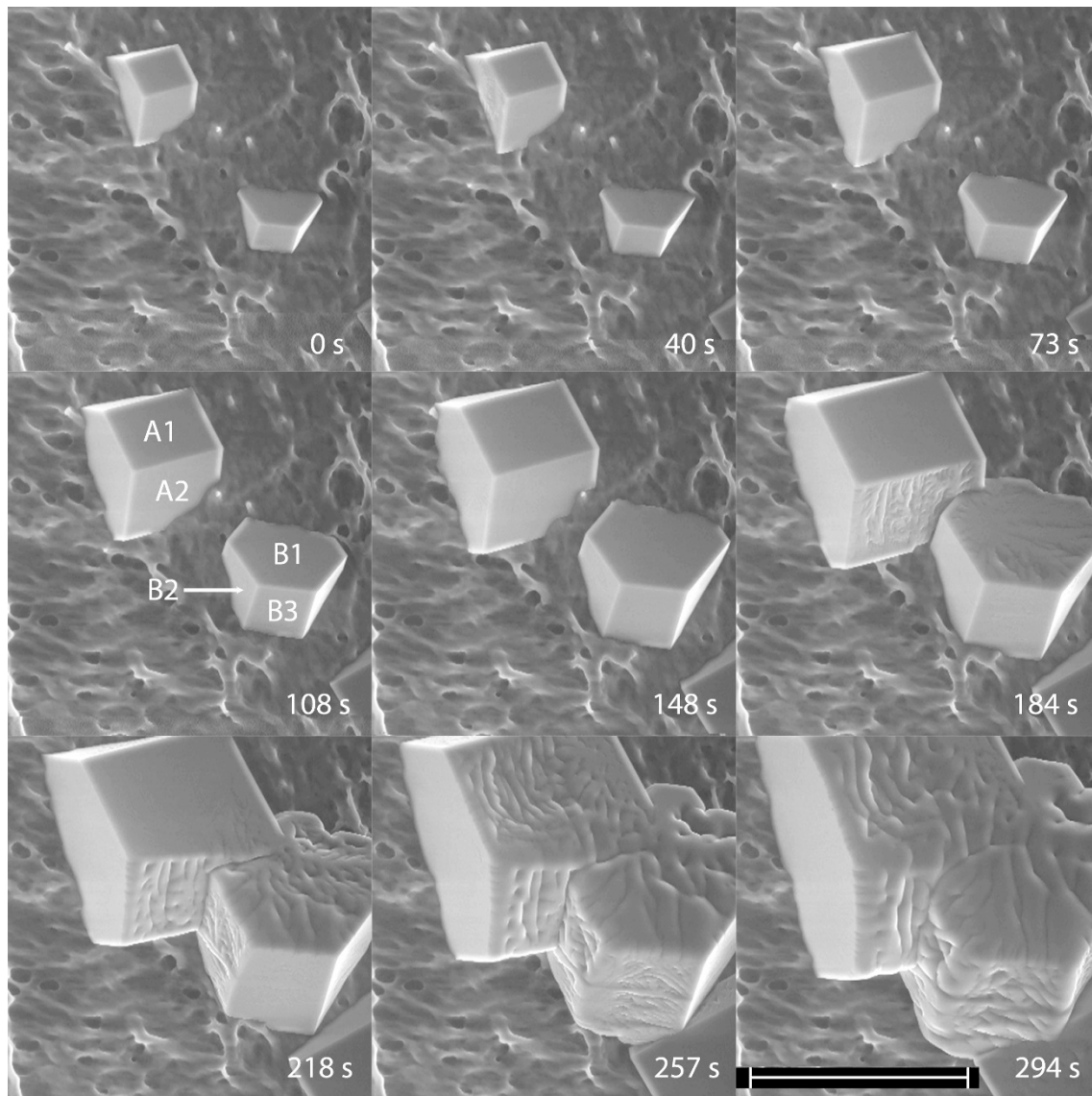
Figure 3.13 Grain boundaries producing ledges

Grain boundaries form as ice crystals interest. The ice surface transitions to nucleate numerous ledged near the grain boundary (Pedersen et al., 2011, Figure 2).
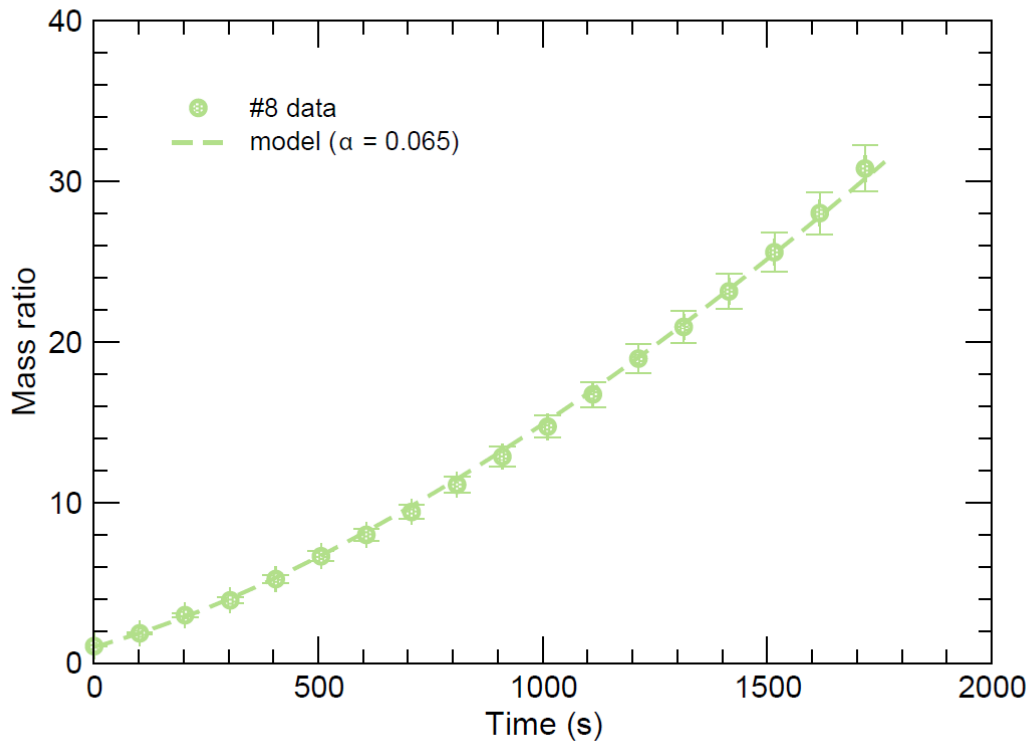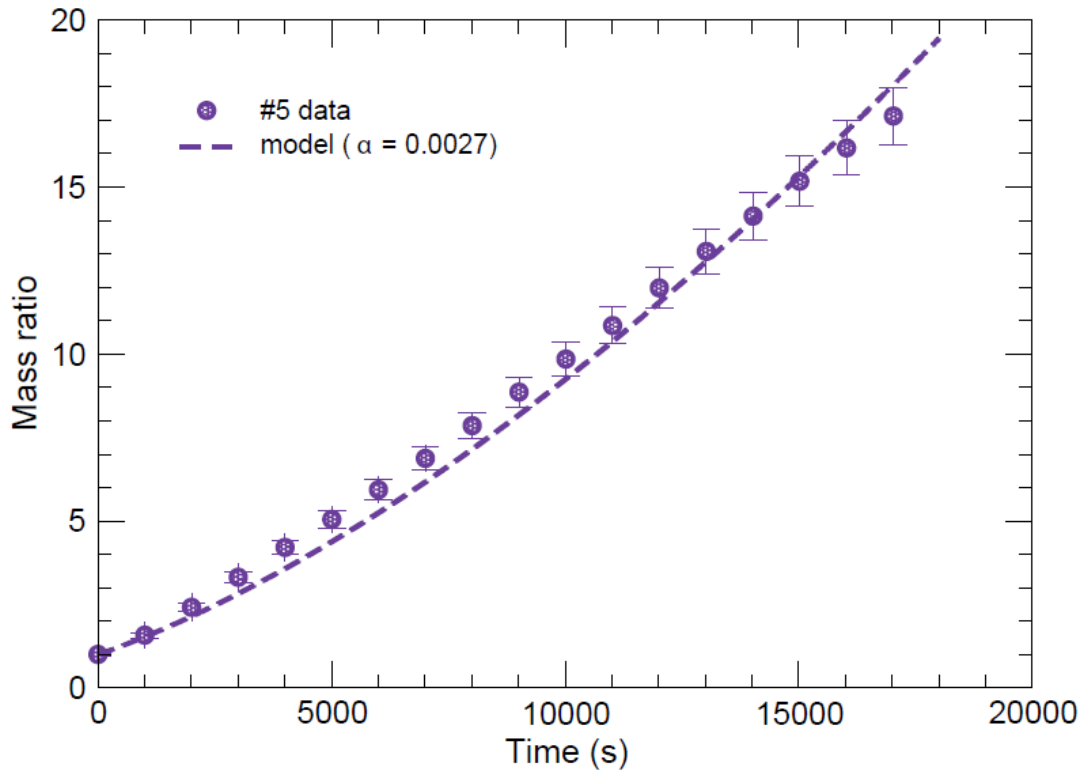
Figure 3.14 Mass ratio timeseries and model fit of particle #8

Displayed is the mass ratio timeseries of particle #8 (points) and the KLAH model's best fit (dashed). This serves an example of the KLAH model fit capturing the data's behavior.
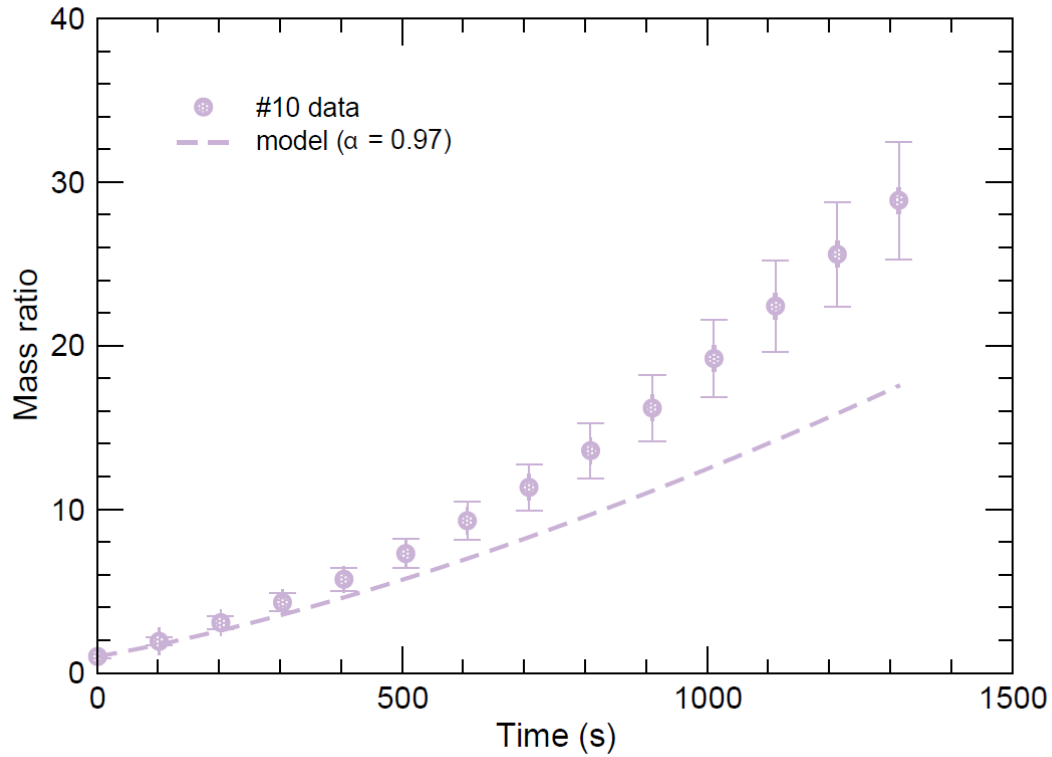
Figure 3.15 Mass ratio timeseries and model fit of particle #10

This is the mass ratio timeseries of particle #10 (points) and its best KLAH model fit (dashed). Despite the model using a deposition coefficient of nearly unity, its simulated growth is much slower than the particle's actual growth. This is an example of the model poorly fitting the data.

Figure 3.16 Mass ratio timeseries and model fit of particle #5

Plotted is the mass ratio timeseries of particle #5 (points) and its modeled fit (dashed). The KLAH model fit matches the data fairly well, but it does not capture the distinct linear trend of the timeseries.
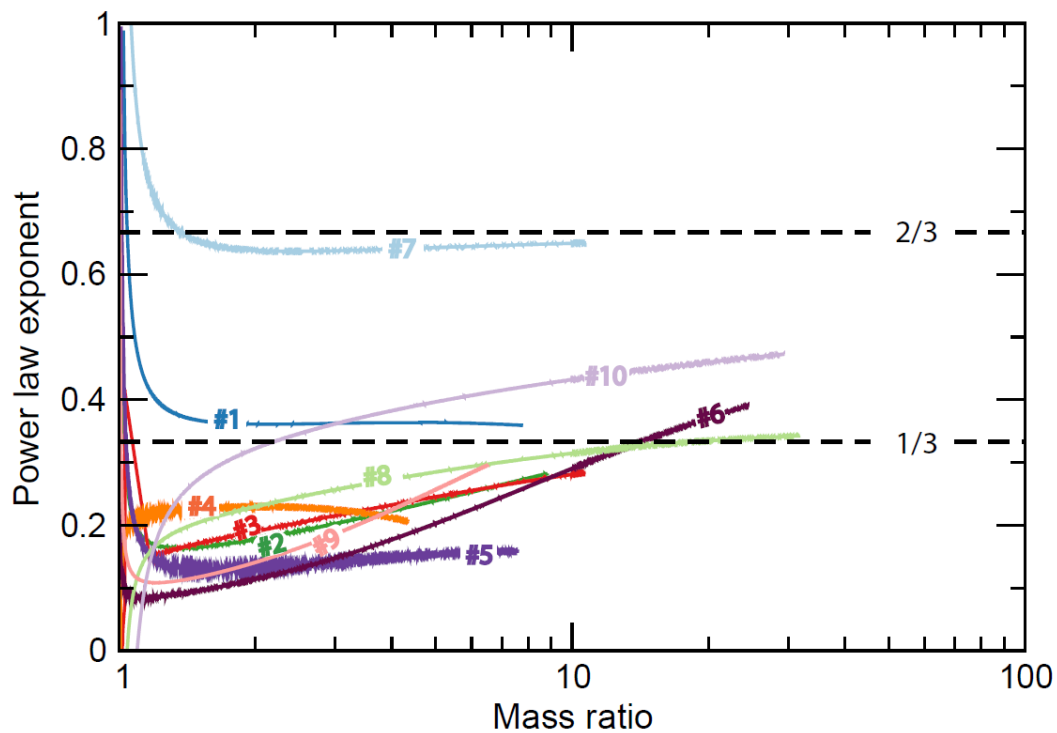
Figure 3.17 Power law analysis of the data

The power law exponent for many of the ice particles falls outside of the expected $1/3 \leq P \leq 2/3$ range. However, particles #1, 6, 7, 8, and 10 have expected P values for some portion of their growth. The remaining particles behave as though they have a variable growth mode parameter M.

Figure 3.18 Power law analysis with the diffusion-kinetics model

(Caption on the following page.)

Figure 3.8 a) If M is constant (solid), the power law produced by the diffusion-kinetic model is within the $1/3 – 2/3$ range, regardless of the environmental conditions. The example plotted is the ambient supersaturation, where increasing S_i causes P to asymptote to $1/3$. If M is variable (dashed), the modeled power law is less than $1/3$, and it decreases with decreasing supersaturation. (Note: The dashed $S_i = 1\%$ power curve descends below -0.2, the minimum on the figure.) **b)** If a particle is columnar, in this case with $S_{crit} = 5.45\%$ on the c-axis and $S_{crit} = 10.9\%$ on the a-axis, then is it possible for P to cross the $1/3$ line. The solid curves correspond to 2D nucleation growth ($M = 15$), the dotted curves represent dislocation growth ($M = 1$), and the dashed curves are again produced with a variable growth mechanism ($M = 1 \rightarrow 10$). Like in (a), the variable-M curves remain below $P = 1/3$. However, when $S_i = 5\%$ (blue), the 2D nucleation case begins below $P = 1/3$ and ends above it. This does not happen at $S_i = 1\%$ or 10%. Also, at every supersaturation value, the dislocation growth curves remain with P only slightly greater than $1/3$. **c)** The normalized diffusivity increases if M is constant, but it decreases if M increases. This plot exemplifies the effective diffusivity power law on the radius (Equation 2.9).
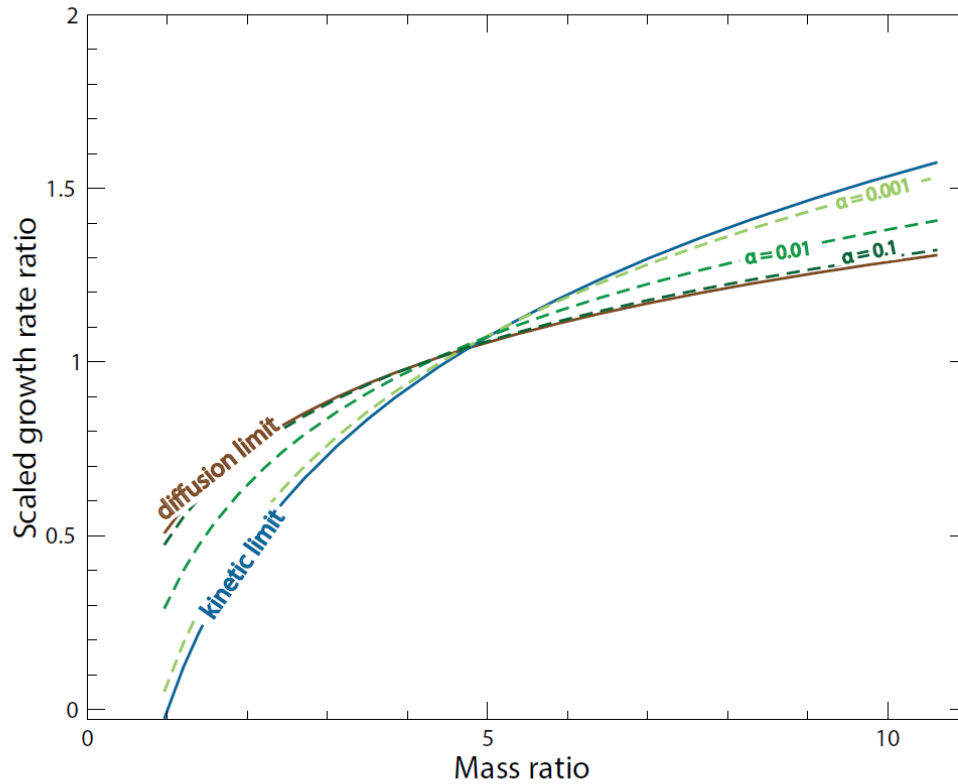
Figure 3.19 Demonstration of scale analysis with the diffusion-kinetics model

Using the scale analysis method, the diffusion limit, kinetic limit, model, and data are directly compared. This example (excluding the data for clarity) demonstrates that the diffusion and kinetic limit curves intersect once, and the constant-M modeled curves pivot about that intersection with a dependence on the deposition coefficient. If M is constant, the model is restrained to those extreme growth modes.
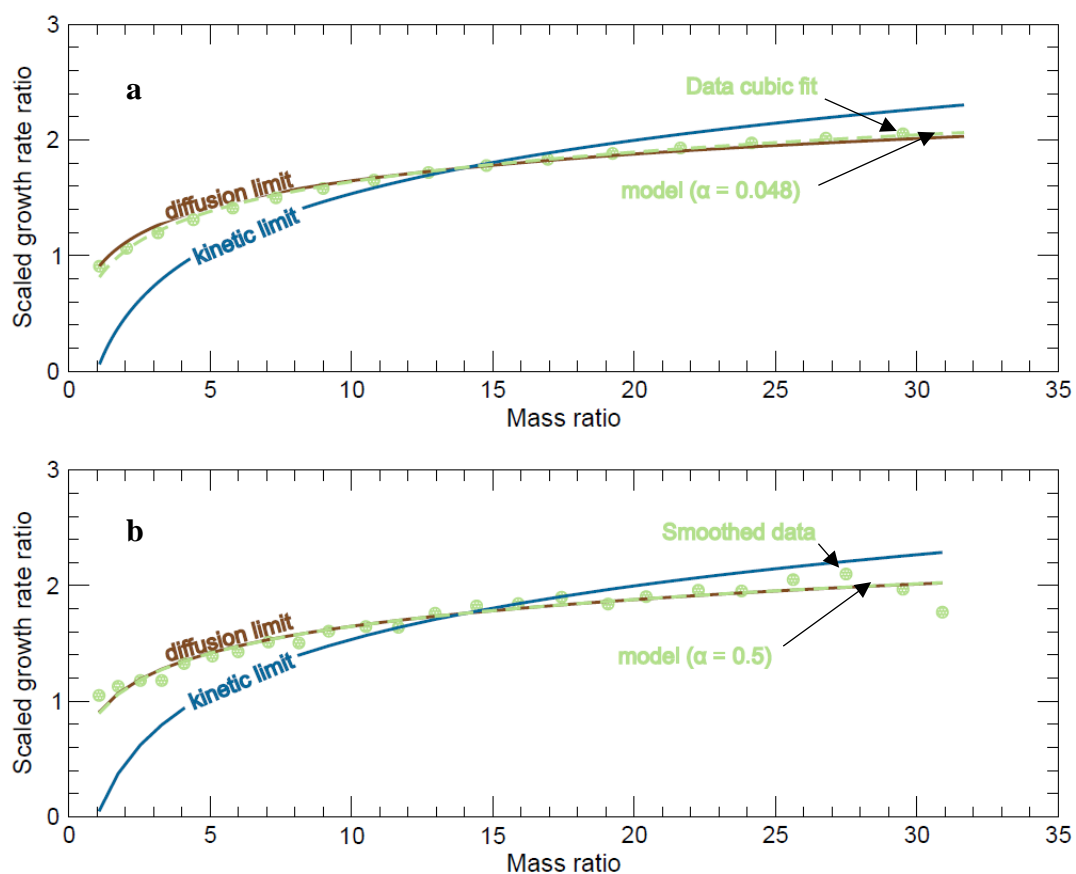
Figure 3.20 Scale analysis of particle #8

Displayed are the scale analysis results for particle #8 from **a)** the cubic fit of the data, and **b)** the smoothed data. The standard diffusion-kinetic model with a constant $M = 10$ fits the data's cubic fit with $\alpha = 0.048$ and the smoothed data with $\alpha = 0.5$. This range covers the deposition coefficient values produced by the original timeseries analysis ($\alpha = 0.065$). Both analysis methods suggest that this ice particle experienced nearly diffusion-limited growth.
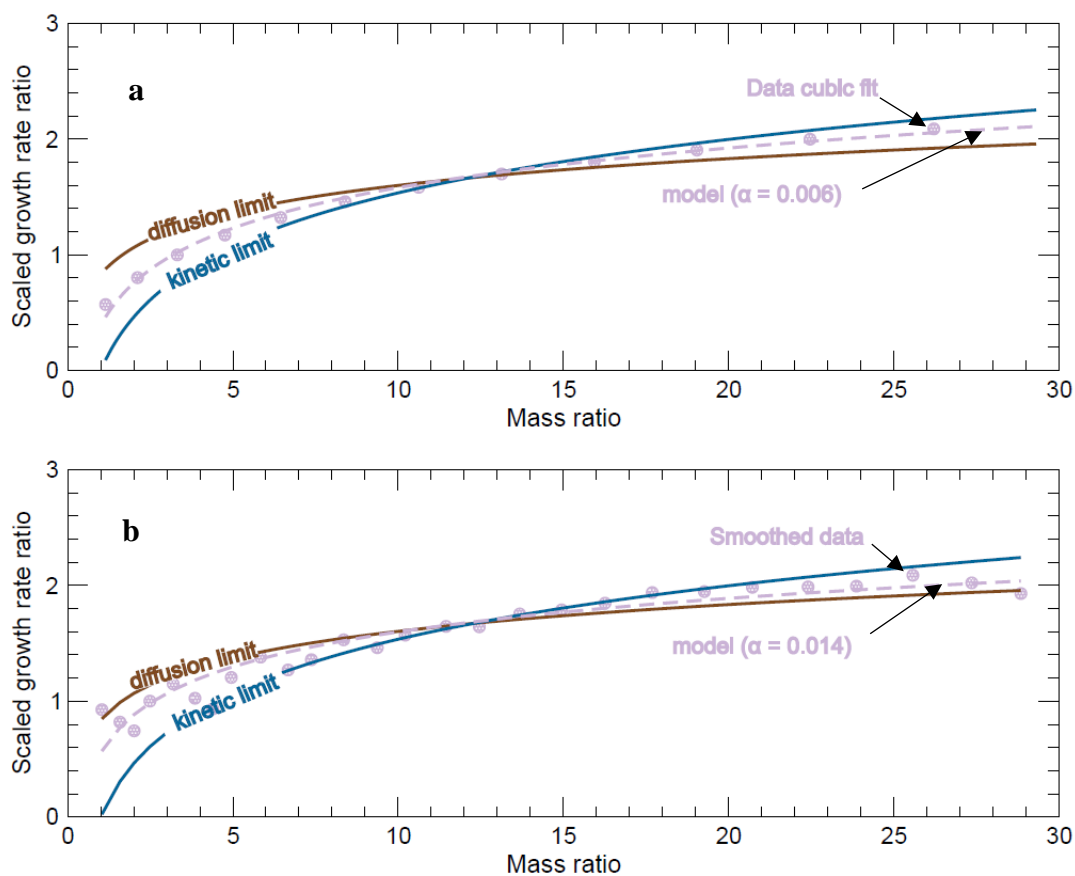
Figure 3.21 Scale analysis of particle #10

Plotted are the scale analysis results for particle #10 from **a)** the cubic fit of the data, and **b)** the smoothed data. The standard diffusion-kinetic model with a constant $M = 10$ fits the data's cubic fit with $\alpha = 0.006$ and the smoothed data with $\alpha = 0.014$. The scale analysis is able to extract a deposition coefficient value while the original timeseries analysis method was not.
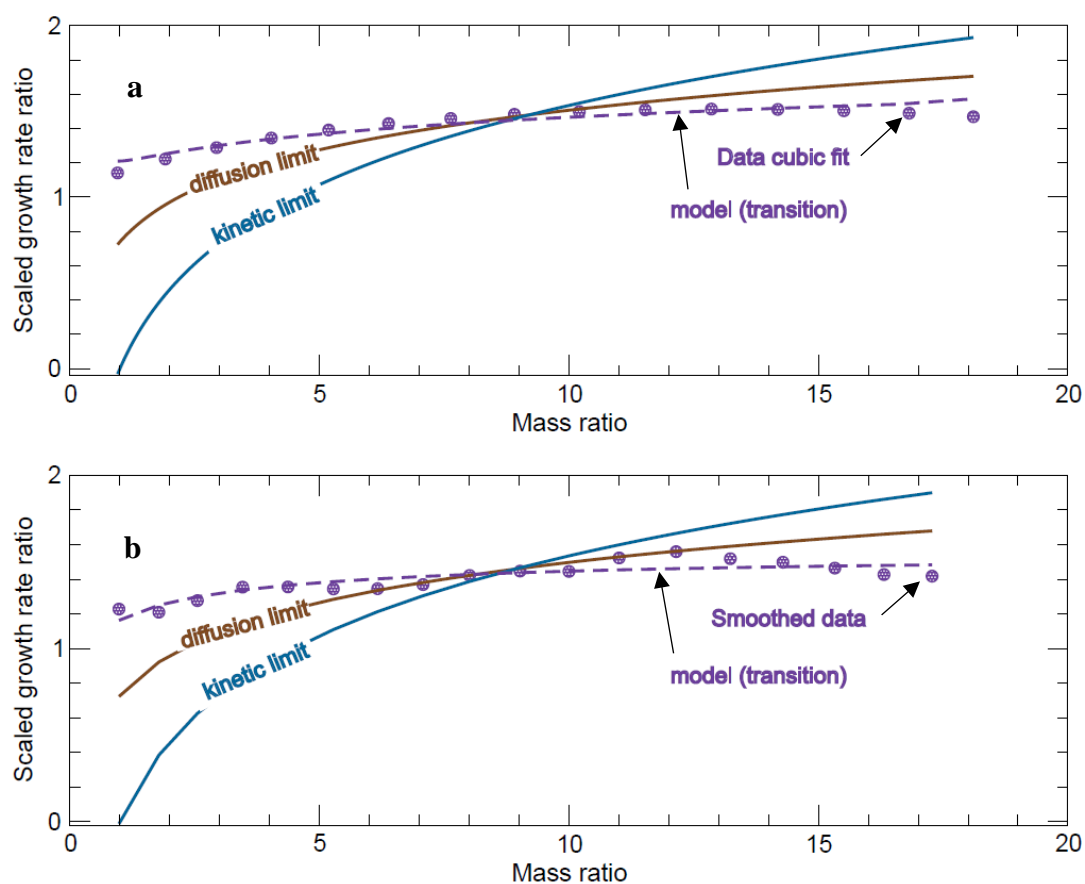
Figure 3.122 Scale analysis of particle #5

Shown are the scale analysis results for particle #5 from **a)** the cubic fit of the data, and **b)** the smoothed data. The data does not fall within the diffusion and kinetic limit boundaries. Modeling this ice particle's growth using $M = 10$, produces a scenario where $\alpha = 0.5$ (not shown). However, modeling with the variable M defined in Equation 3.1 produces a curve that behaves much like the data by exiting the boundaries set with a constant growth mode.
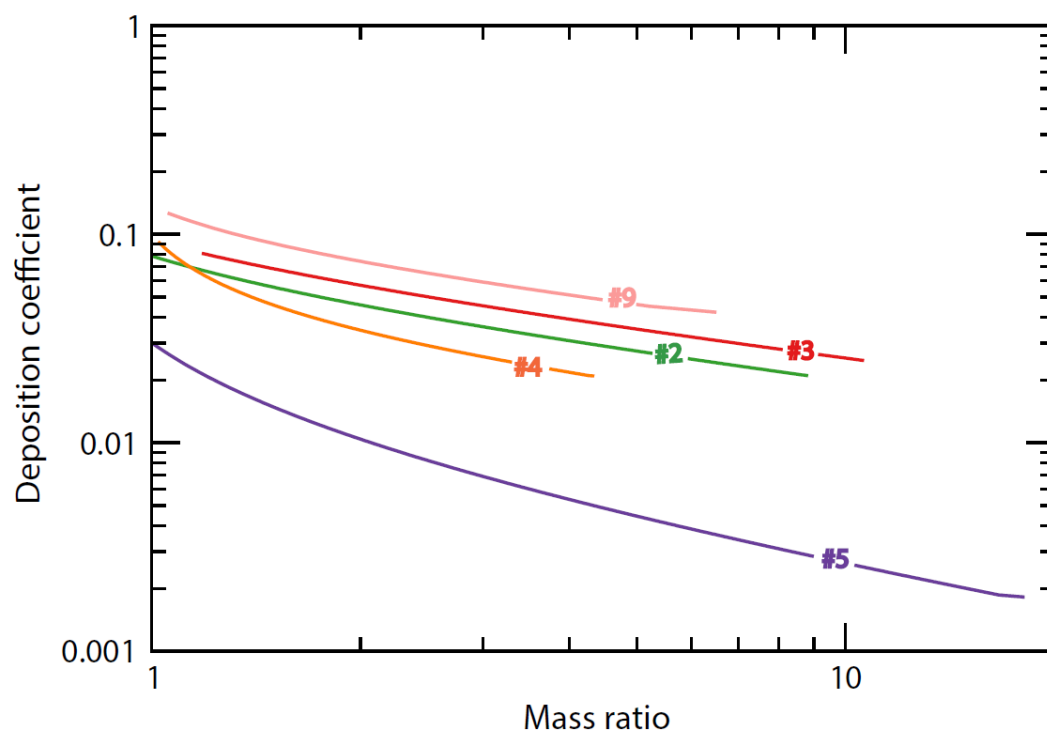
Figure 3.23 Transitioning deposition coefficients

The modeled deposition coefficient rapidly declines as particles with surface transitions grow. Note that the deposition coefficient for particle #5 spans more than an order of magnitude. The initial and final α values for particles #2, 3, 4, 5, and 9 are listed in Table 3.6.
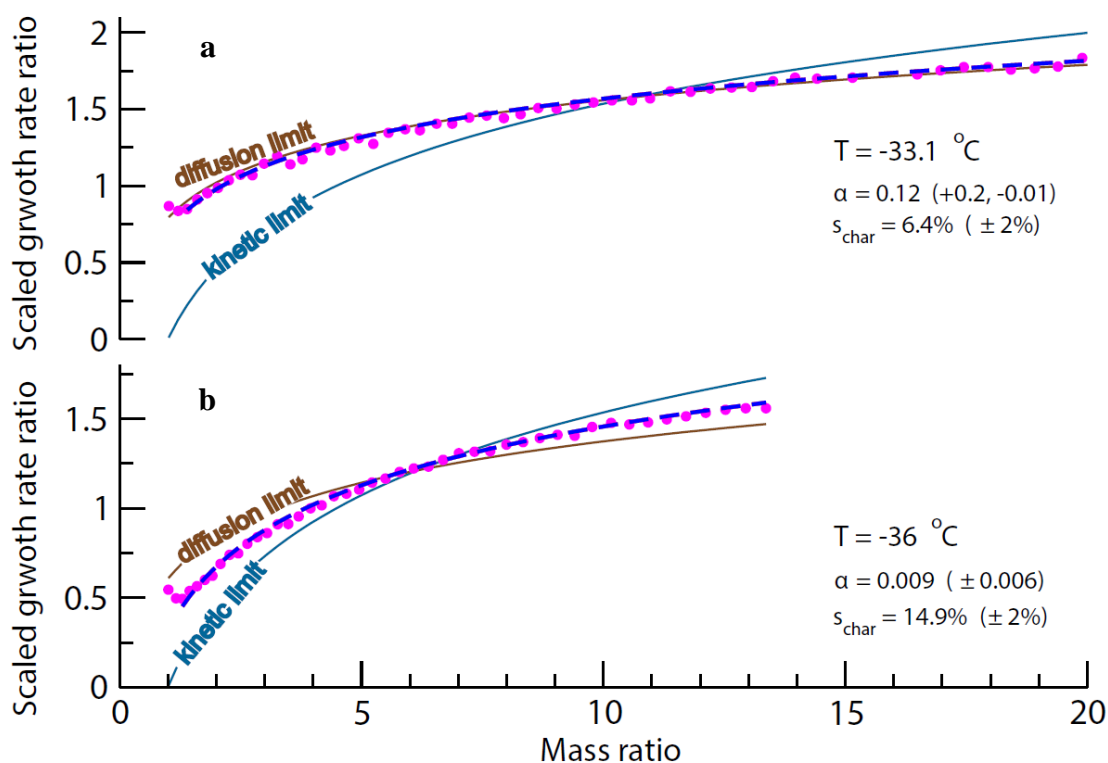
Figure 3.24 Scale analysis of Harrison et al. (2016) data

Re-analysis of raw data from Harrison et al. (2016) using the scale analysis method accurately fits the heterogenous nucleation data. The fits clearly show the difference between a particle with **(a)** diffusion-limited growth and **(b)** diffusion-kinetics limited growth (Harrington et al., 2018).
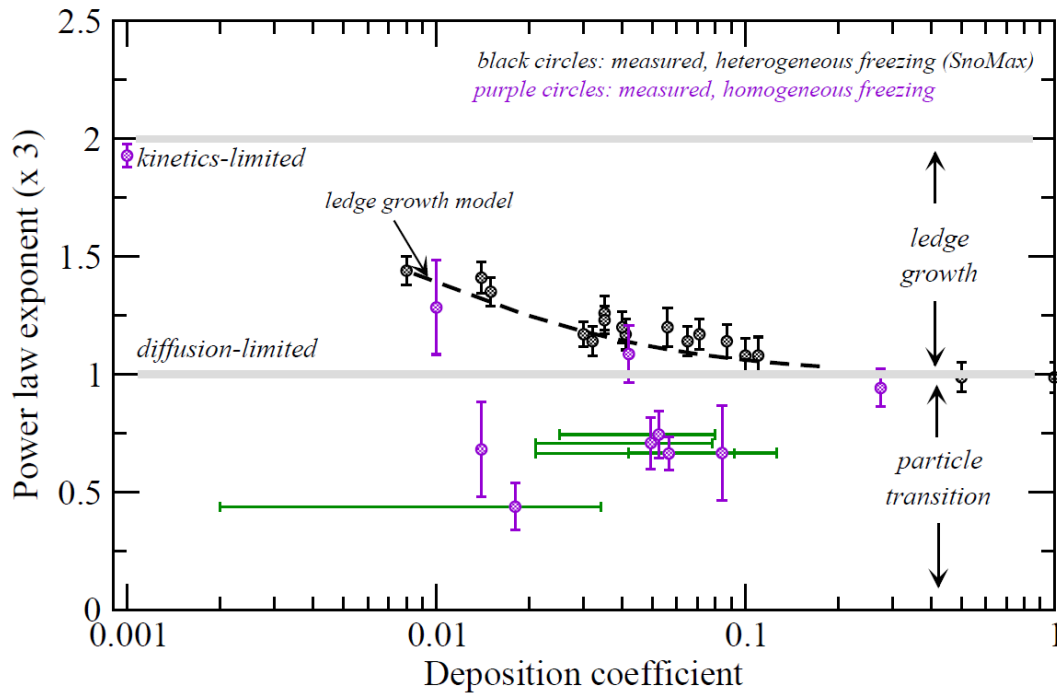
Figure 3.25 Plot of the deposition coefficient v. the power law

The scale analysis and power law analysis results are directly compared. The black points are from heterogeneously nucleated particles (Harrison et al., 2016), and the purple points are from homogeneously nucleated particles (this work). Uncertainty ranges are taken from the initial and final power laws on the timeseries data. Note that the green horizontal ranges are not uncertainties; rather, they are the ranges over which the deposition coefficients change as the surfaces transition. Also, be aware that the y-axis represents $P \times 3$. Therefore, the y = 1 line now applies to diffusion limited growth, and y = 2 to kinetics-limited growth. Curiously, most of the non-transitioning particles cluster around the plot of the classical ledge growth model (Harrington et al., 2018).

Gwenore Pokrifka
Academic Vita

Department of Meteorology
The Pennsylvania State University
502 Walker Building
University Park, PA 16802
Phone: (724) 575-2938
Email: gfp5025@psu.edu

Education

M.S	Meteorology	Penn State University University Park, PA	May 2018
B.S.	Meteorology (Honors student)	Penn State University University Park, PA	May 2018
Minor	Anthropology	Penn State University University Park, PA	May 2018

Research and Teaching Experience

May 2017 - Present	Graduate Research Assistant, Department of Meteorology, Penn State University
May – August 2016	NSF Research Experience for Undergraduate Internship, Department of Meteorology, Penn State University

Professional Activities and Memberships

2016 - Present	Member of Chi Epsilon Pi, National Meteorology Honor Society

Honors and Awards:

2018	EMSAGE Laureate
2015 / 2016 – 2016 / 2017	Hans A. Panofsky Scholarship
2016 / 2017	Class of 1922 Memorial Scholarship
2015 / 2016	Sophia Elizabeth Kumpf Scholarship for Women
2015 / 2016 – 2016 / 2017	Rita Ebner Caste Memorial Scholarship
2013 / 2014 – 2014 / 2015	Leslie Clarkson Pyle and Anna C. Pyle Memorial Scholarship
2013 / 2014	President's Freshman Award

Publications

Pokrifka, G., A, Moyle, M. Hanson, and J.Y. Harrington, 2018: Estimating the deposition coefficient and surface attachment kinetics from measurements of ice crystal mass growth from the vapor. In preparation for *J. Atmos. Sci*